

---

# Towards Infinitely Long Neural Simulations: Self-Refining Neural Surrogate Models for Dynamical Systems

---

Qi Liu<sup>1</sup> Laure Zanna<sup>1</sup> Joan Bruna<sup>1</sup>

## Abstract

Recent advances in autoregressive neural surrogate models have enabled orders-of-magnitude speedups in simulating dynamical systems. However, autoregressive models are generally prone to *distribution drift*: compounding errors in autoregressive rollouts that severely degrade generation quality over long time horizons. Existing work attempts to address this issue by implicitly leveraging the inherent trade-off between short-time accuracy and long-time consistency through hyperparameter tuning. In this work, we introduce a unifying mathematical framework that makes this tradeoff explicit, formalizing and generalizing hyperparameter-based strategies in existing approaches. Within this framework, we propose a robust, hyperparameter-free model implemented as a conditional diffusion model that balances short-time fidelity with long-time consistency by construction. Our model, *Self-refining Neural Surrogate model (SNS)*, can be implemented as a standalone model that refines its own autoregressive outputs or as a complementary model to existing neural surrogates to ensure long-time consistency. We also demonstrate the numerical feasibility of SNS through high-fidelity simulations of complex dynamical systems over arbitrarily long time horizons.

## 1. Introduction

Understanding and simulating physical systems is a foundational aspect of many scientific and engineering fields, including earth system modeling, neural science, and robotics (Lorenz, 1963; Chariker et al., 2016; Ijspeert et al., 2013). Dynamical systems are the major mathematical tools used to model these systems, which describe how the states of the system evolve over time through partial differential equa-

tions (PDEs). Traditionally, these PDEs are solved numerically, which requires fine spatial discretizations to capture the local dynamics accurately. However, fine spatial discretization imposes constraints on the temporal discretization as well, such as the Courant-Friedrichs-Lewy (*CFL*) condition for numerical stability, leading to unfeasible computational costs (Lewy et al., 1928).

Deep learning techniques have been incorporated in various ways to address this challenge. In particular, autoregressive neural surrogate models have been deployed to replace numerical schemes entirely (Li et al., 2020; Stachenfeld et al., 2022; Kochkov et al., 2024). Autoregressive neural surrogates, compared to their numerical counterparts, can achieve orders of magnitude computational speedups by reducing the number of function evaluations and leveraging parallel processing on GPUs (Kurth et al., 2023). These neural surrogate models are being applied to weather forecasting (Pathak et al., 2022; Bi et al., 2023) and climate modeling (Kochkov et al., 2024; Subel & Zanna, 2024; Dheeshjith et al., 2025).

Autoregressive models take their own outputs as inputs. Despite the tremendous success of autoregressive neural surrogate models in achieving short-term accuracy, the performance tends to degenerate over longer time horizons (Chattopadhyay et al., 2023; Bonavita, 2024; Parthipan et al., 2024; Bach et al., 2024). Autoregressive models are prone to *distribution drift*: they are trained on data from a distribution, but there is no guarantee that their outputs will remain within it during inference. This motivates decomposing the risk of an autoregressive model into *conditional approximation error* and *out-of-distribution (OOD) error*. Many existing efforts to enhance long rollouts’ performance implicitly balance a tradeoff between these two errors. However, most prior work relies on heuristic strategies that yield strong empirical results but offer limited theoretical justification.

In this work, we will provide a general mathematical framework, based on *multi-noise-level denoising oracle*, that explicitly accounts for the trade-off between *conditional approximation error* and *OOD error*. Estimators of the *multi-noise-level denoising oracle* create a flexible design space for seeking an optimal balance between the two errors. We

<sup>1</sup>Courant Institute School of Mathematics, Computing, and Data Science, New York University, USA. Correspondence to: Qi Liu <ql2221@nyu.edu>.

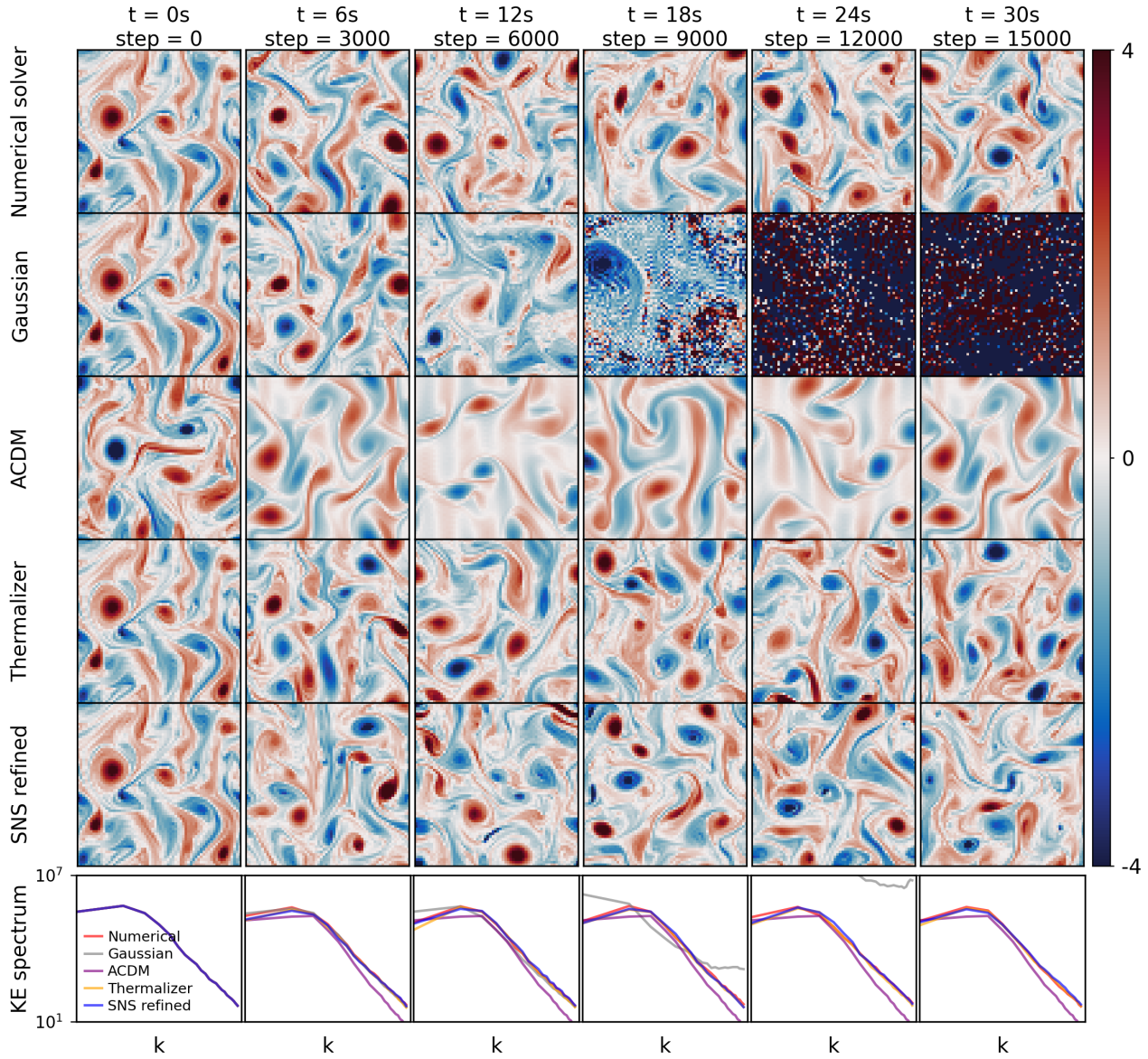


Figure 1. *Top 5 rows:* Vorticity fields of the Kolmogorov flow from a numerical solver, Gaussian approximation of the transition density, ACDM with 200 denoising steps, *Thermalizer* and *SNS refined* trajectories for Kolmogorov flow over a trajectory of 15,000 steps. *Bottom row:* kinetic energy spectra at each timestep, averaged over 20 randomly initialized trajectories.

propose our model, *Self-refining Neural Surrogate model (SNS)*, which seeks to achieve the optimal balance between the errors within this framework. During inference, *SNS* dynamically determines the noise level for the conditioning and the denoising strategies. We implement *SNS* as a conditional diffusion model (Sohl-Dickstein et al., 2015; Song et al., 2020) trained on a denoising diffusion probabilistic model (DDPM) style denoising score matching objective (Ho et al., 2020). *SNS* can be used as a standalone model that refines its own output or as a complementary model alongside existing neural surrogates to enhance long-term performance. We demonstrate the numerical feasibility of *SNS* through high fidelity simulations over a long time horizon.

### Main contributions

We propose the *multi-noise-level denoising oracle* with an explicit representation of the approximation-*OOD* tradeoff to transform a heuristic goal into a concrete, learnable objective. We present our *self-refining neural surrogate* model that seeks to dynamically balance the tradeoff within this framework.

## 2. Related Work

### Diffusion models as surrogates

Conditional diffusion models have been utilized by *GenCast* (Kohl et al., 2024) and autoregressive conditional diffusion model (*ACDM*) (Price et al., 2023) for probabilistic simulations of dynamical systems. *ACDM* follows the *Conditional Diffusive Estimator* (CDiffE) framework (Batzolis et al., 2021), in which the conditioning variables and target outputs are jointly diffused. In contrast, *GenCast* conditions on clean and unperturbed inputs, following prior work on conditional diffusion models (Song & Ermon, 2019; Karras et al., 2022). Our approach, *SNS*, is also implemented as a conditional diffusion model; however, a key distinction is that both *ACDM* and *GenCast* condition their generation on previous autoregressive outputs under the assumption that these inputs remain in distribution. As a result, both models remain susceptible to *distribution drift* arising from the accumulation of out-of-distribution (OOD) errors during rollout.

A well-known limitation of diffusion-based models (including ours) is their long inference time, which arises from degradation in sample quality when the reverse process is insufficiently discretized. Consequently, substantial effort has been devoted to accelerate diffusion inference, including consistency models (Song et al.) and progressive distillation techniques (Salimans & Ho, 2022). To the best of our knowledge, these approaches have not yet been applied to autoregressive conditional diffusion models for faster simulation.

Several recent works propose alternative strategies to reduce computational cost. (Shehata et al., 2025) accelerates inference by skipping portions, especially the end, of the reverse process via Tweedie’s formula. *Dyffusion* (Cachay et al., 2023) avoids solving the reverse stochastic differential equation by replacing the forward and backward processes with a learned interpolator and forecaster. For high-dimensional spaces, (Gao et al., 2024) reduces inference cost by performing diffusion in a learned low-dimensional latent space. *PDE-Refiner* (Lippe et al., 2023), one of the first diffusion-based methods for PDE modeling, mitigates computational overhead by acting as a complementary refinement module on top of a point-wise autoregressive predictor. Similar to *PDE-Refiner*, our model, *SNS*, can also work around the computational cost of diffusion-based approaches by dynamically truncating the initial stages of the reverse process with a rough next state estimate from a point-wise autoregressive predictor.

### Mitigating Distribution Drift

Recent work has focused on mitigating *distribution drift* in autoregressive models by exploiting properties of the stationary distribution (Jiang et al., 2023; Schiff et al., 2024; Pedersen et al., 2025). In particular, the *Thermalizer* framework (Pedersen et al., 2025), which dynamically maps out-of-distribution samples back to the stationary distribution through a diffusion model, is conceptually similar to our model. However, *Thermalizer*’s objective is solely to ensure long-time stability while we consider the optimal tradeoff one can make to ensure stability while respecting temporal dynamics. Prior work by (Stachenfeld et al., 2022) demonstrated that employing a non-degenerate Gaussian approximation to the transition density improves long-time consistency. Moreover, unrolling this Gaussian approximation and minimizing mean squared error (MSE) over multiple time steps has been shown to further enhance long-horizon performance (Lusch et al., 2018; Um et al., 2020; Vlachas et al., 2020). Conditioning the model on a larger temporal context has also proven effective in reducing *distribution drift* (Nathaniel & Gentine, 2026; Zhang et al., 2025). While our approach offers an alternative mechanism for extending the consistency horizon of simulations, our primary objective is to provide theoretical insight into the conditions and mechanisms that enable truly infinite-length generation.

## 3. Problem Setup

### Background

Consider a dynamical system in  $\mathbb{R}^n$  with an unknown forward operator  $\mathcal{F} : \mathbb{R}^n \rightarrow \mathbb{R}^n$  and initial condition  $\mathbf{x}_0$ , s.t.

$$\partial_t \mathbf{x}(t) = \mathcal{F}(\mathbf{x}(t), t), \quad \mathbf{x}(0) = \mathbf{x}_0.$$

For a typical time scale  $\Delta t$ , we denote  $\{\mathbf{x}_t\}_{t \in \mathbb{N}}$  to be the time-discretized snapshots of the system where  $\mathbf{x}_t = \mathbf{x}(t \Delta t)$ . Given samples of such snapshots as training data, the goal is to generate dynamically consistent trajectories given new initial conditions.

The operator  $\mathcal{F}$  is, in general, nonlinear and exhibits chaotic dynamics, i.e., small perturbations in initial states evolve to states that are considerably different (Lorenz, 1963). To account for the sensitivity to uncertainty in initial conditions and numerical discretization errors, it is more appropriate to adopt a probabilistic framework of the system. We can view  $\{\mathbf{x}_t\}_{t \in \mathbb{N}}$  as a discrete realization of a continuous time Markovian stochastic process,  $\{\mathbf{X}_\tau\}_{\tau \in \mathbb{R}}$ , i.e.  $\mathbf{x}_t = \mathbf{X}_{t\Delta\tau}(\omega)$ . We denote the path density of the process  $p_t := p(\mathbf{x}_0, \dots, \mathbf{x}_t)$  which satisfies the recurrence relation:  $p_{t+1} = p(\mathbf{x}_{t+1}, (t+1)\Delta\tau | \mathbf{x}_t, t\Delta\tau) p_t$ , where the transition density  $p(\mathbf{x}_{t+1}, (t+1)\Delta\tau | \mathbf{x}_t, t\Delta\tau)$  is the conditional distribution of  $\mathbf{X}_{(t+1)\Delta\tau}$  given  $\mathbf{X}_{t\Delta\tau} = \mathbf{x}_t$ . Here we assume that the Markov transition kernel admits a density, i.e.  $\mathcal{Q}(\mathbf{x}_t, d(\mathbf{x}_{t+1})) = p(\mathbf{x}_{t+1}, (t+1)\Delta\tau | \mathbf{x}_t, t\Delta\tau) d\mathbf{x}_{t+1}$ . In addition, if the system is autonomous and ergodic, the transition density reduces to  $p(\mathbf{x}_{t+1} | \mathbf{x}_t)$  and a unique limiting distribution exists which coincides with the stationary distribution. We denote this distribution as  $\mu := \mu_\infty = \lim_{t \rightarrow \infty} \mu_t$ , where  $\mu_t$  is the marginal distribution of  $\mathbf{x}_t$ , i.e.  $\mu_t = \mathcal{Q}_{\#}^t(\mathbf{x}_0, \mathbf{x}_t)p(\mathbf{x}_0)$ . We choose to focus on ergodic systems in this work, but the method can be extended to time-dependent systems as well. Because of the Markovian properties, it suffices to learn the one-step conditional distribution and generate new trajectories by sampling from the learned distribution,  $\hat{p}$ , autoregressively as follows: given  $\mathbf{x}_0$ , sample  $\hat{\mathbf{x}}_{t+1} \sim \hat{p}(\mathbf{x}_{t+1} | \hat{\mathbf{x}}_t)$  recursively with  $\hat{\mathbf{x}}_0 = \mathbf{x}_0$ .

### Modeling transition density via diffusion models

The transition density has the property that  $p(\mathbf{x}_{t+1} | \mathbf{x}_t) = \delta(\mathbf{x}_{t+1} - \mathbf{x}_t)$  as  $\Delta\tau \rightarrow 0$ , i.e. the transition density is a Dirac mass at the current snapshot without time evolution. So in the asymptotics of  $\Delta\tau \ll 1$ , it is reasonable to approximate the transition density with a ‘‘sharp’’ gaussian distribution:  $p(\mathbf{x}_{t+1} | \mathbf{x}_t) = \mathcal{N}(\mathbf{x}_{t+1}; \mathcal{F}(\mathbf{x}_t), \Sigma(\Delta\tau))$  where  $\Sigma(\Delta\tau)$  has vanishing spectral radius as  $\Delta\tau \rightarrow 0$ . At a fixed time discretization  $\Delta\tau$ , both the mean and the covariance matrix can be learned, and we denote the learned Gaussian kernel:  $\hat{p}(\mathbf{x}_{t+1} | \mathbf{x}_t) = \mathcal{N}(\mathbf{x}_{t+1}; \mathcal{F}_\theta(\mathbf{x}_t), \Sigma_\theta)$ . We refer to this approach as the Gaussian approximation and provide more details about the learning objective in B.2.

Conditional diffusion models can also be used to generate samples from the transition density  $p(\mathbf{x}_t | \mathbf{x}_{t-1})$ . Diffusion models (Sohl-Dickstein et al., 2015; Ho et al., 2020; Song et al., 2020), when first proposed, enable transport between a source distribution  $p^S$ , usually Gaussian, and an unconditional target distribution  $p^0$  by a forward process and a

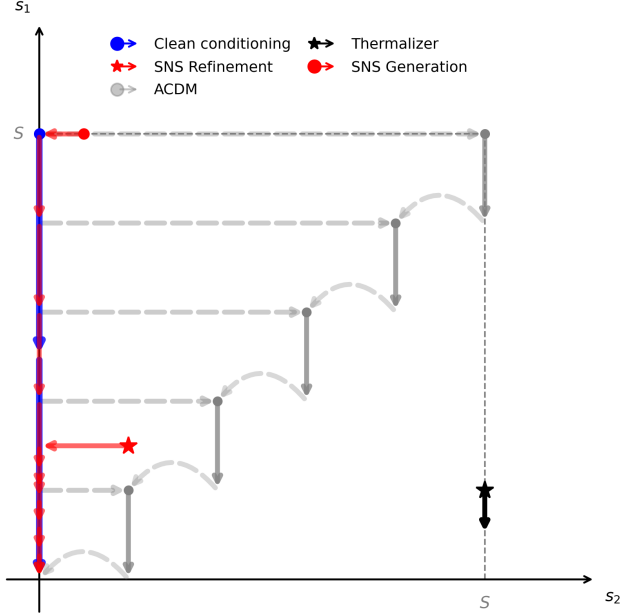


Figure 2. Phase space for the forward and reverse process : Moving to the right and moving to the left corresponds to the forward process and the reverse process for  $\mathbf{x}_{t-1}$ . Moving up and down corresponds to the forward and the reverse process for  $\mathbf{x}_t$ , respectively. The dashed curved arrows represent a jump in the reverse process.

learned reverse process. We will use  $s$  for diffusion time as a superscript, which is independent of the physical time  $t$ . Given  $\mathbf{x}^0 \sim p^0$ , the forward process:

$$d\mathbf{x}^s = \mathbf{f}(\mathbf{x}^s, s)ds + g(s)d\mathbf{w}^s, \quad s \in [0, S]$$

is a stochastic process that starts at the target distribution and ends at the source distribution, i.e.  $\mathbf{x}^0 \sim p^0, \mathbf{x}^S \sim p^S$ . One could generate new samples from the target distribution by solving the SDE associated with the reverse process backwards in time (from  $s = S$  to  $s = 0$ ) with initial condition  $\mathbf{x}^S \sim p^1$  (Anderson, 1982):

$$d\mathbf{x}^s = [\mathbf{f}(\mathbf{x}^s, s) - g(s)^2 \nabla \log p^s(\mathbf{x}^s)]ds + g(s)d\bar{\mathbf{w}}^s$$

where  $p^s(\mathbf{x}^s)$  is the marginal density of  $\mathbf{x}^s$ . Solving the reverse SDE requires estimating the score,  $\mathbf{s}_\theta \approx \nabla \log p^s(\mathbf{x}^s)$ , which can be done via various training objectives. In particular, (Ho et al., 2020) proposed a denoising objective. Defining the denoising oracle as:

$$D(\mathbf{x}^s, s) := \mathbb{E}[\mathbf{x} | \mathbf{x}^s] \quad (1)$$

Tweedie’s formula (Robbins, 1992), relates the denoising oracle to the score explicitly via:  $\nabla \log p^s(\mathbf{x}^s) = -\sigma_s^{-2}(\mathbf{x}^s - D(\mathbf{x}^s, s))$ , where  $\sigma_s^2 = \int_0^s g(s')^2 ds'$ .

Conditional diffusion models enable sampling from a conditional distribution,  $p(\mathbf{x} | \mathbf{c})$ . One could consider evolving

the conditional reverse process SDE:

$$d\mathbf{x}^s = [\mathbf{f}(\mathbf{x}^s, s) - g(s)^2 \nabla \log p^s(\mathbf{x}^s | \mathbf{c})] ds + g(s) d\bar{\mathbf{w}}^s$$

to generate samples from  $p(\mathbf{x} | \mathbf{c})$ . Multiple methods to estimate the conditional score  $\nabla \log p^s(\mathbf{x}^s | \mathbf{c})$  have been proposed, such as via Bayes’s rule (Dhariwal & Nichol, 2021), classifier-free guidance (Ho & Salimans, 2022), and conditional score matching. In particular, (Batzolis et al., 2021) considered the loss function,

$$\mathcal{L}(\theta) = \frac{1}{2} \mathbb{E}_{s \sim \mathcal{U}(0, S)} \mathbb{E}_{\mathbf{x}_0, \mathbf{x}_s \sim p_s(\mathbf{x}_s | \mathbf{x}_0)} \left[ \lambda(t) \left\| \nabla \log p^s(\mathbf{x}^s | \mathbf{x}^0) - \mathbf{s}_\theta(\mathbf{x}_s, \mathbf{c}, s) \right\|_2^2 \right].$$

and showed that the minimizer of the above loss function coincides with the minimizer of the loss function with the score  $\nabla \log p^s(\mathbf{x}^s | \mathbf{x}^0)$  replaced by the conditional score:  $\nabla \log p^s(\mathbf{x}^s | \mathbf{c})$ . Further more, one could consider learning the score of the annealed conditional distribution  $\nabla \log p^s(\mathbf{x}^s | \mathbf{c}^s)$ , which coincides with the score of the joint distribution  $p^s(\mathbf{x}^s, \mathbf{c}^s)$ , and use it as an approximation to  $\nabla \log p^s(\mathbf{x}^s | \mathbf{c})$  as we will discuss in Section 4.1.

### Distribution drift in autoregressive models

To make the distinction between short-horizon prediction accuracy and long-horizon physical consistency precise, it is useful to consider a finite-dimensional Markov system. Let  $M$  denote the true transition matrix and  $\hat{M}$  its learned approximation, with stationary distributions  $\mu$  and  $\hat{\mu}$ , i.e. the Perron (left) eigenvectors of  $M$ , and  $\hat{M}$ , respectively. This naturally leads to two distinct notions of error.

First, the *conditional approximation error* measures how well one-step transitions are approximated under the true stationary distribution:

$$\mathcal{E}_{\text{cond}} = \sum_i \mu_i \mathcal{D}(M_i \| \hat{M}_i),$$

where  $M_i$  denotes the  $i$ -th row of  $M$  and  $\mathcal{D}$  is a divergence such as KL or total variation. And  $\mu_i$  is the  $i$ -th component of  $\mu$ . Second, the *out-of-distribution (OOD) error* measures the discrepancy between the stationary distributions induced by the true and learned transition density, with the same or possibly different divergence,  $\tilde{\mathcal{D}}$ :

$$\mathcal{E}_{\text{uncond}} = \tilde{\mathcal{D}}(\mu \| \hat{\mu}).$$

While the *conditional approximation error* captures one-step accuracy with in-distribution conditioning, the unconditional prediction error governs long-horizon rollout behavior. Noting that the *conditional approximation error* is a metric on conditional distributions and the *OOD error* is a metric on marginal distributions, any candidate approximation

$\hat{M}$  immediately faces an inherent tradeoff between accurately reconstructing short-time dynamics and maintaining long-time consistency. The minimizer of the *conditional approximation error*, by definition, has to condition on an unperturbed conditioning since any corruption of the conditioning decreases the mutual information between the two variables (Appendix C). Thus, conditional generation on the exact previous state enables accurate approximation of the one-step transition density  $p(\mathbf{x}_t | \mathbf{x}_{t-1})$ . However, even small errors in the conditioning state accumulate during rollouts, leading to *distribution drift*. This mechanism underlies the linear growth of pathwise KL divergence over time. (Pedersen et al., 2025) Conversely, weakening the dependence on the conditioning state improves robustness by biasing generation towards the marginal or stationary distribution, but at the cost of accuracy in modeling the temporal dynamics.

This tradeoff can be formalized by interpolating between conditional and marginal distributions. Introducing noise into the conditioning variable yields a family of intermediate conditional distributions  $\{p^{s_2}(\mathbf{x}_t | \mathbf{x}_{t-1}^{s_2})\}_{s_2 \in [0, S]}$ , which recover the exact transition density in the limit  $s_2 \rightarrow 0$  and marginal density  $p(\mathbf{x}_t)$  as  $s_2 \rightarrow S$ . Therefore, the choice of noise level directly controls the tradeoff between temporal fidelity and long-term stability.

Most existing approaches implicitly select a fixed operating point along this tradeoff curve through hyperparameters or architectural choices. In contrast, our approach explicitly models the full phase space via a *multi-noise-level denoising oracle*, enabling adaptive selection of the appropriate balance during inference.

## 4. Methodology

### 4.1. Multi-noise-level denoising oracle

Denoting  $\mathbf{y}_t := (\mathbf{x}_t, \mathbf{x}_{t-1})$ , we define the *multi-noise-level denoising oracle* to be the conditional expectation:

$$\mathbf{D}(\mathbf{x}_t^{s_1}, \mathbf{x}_{t-1}^{s_2}) := \mathbb{E}_{\mathbf{x}_t, \mathbf{x}_{t-1} \sim p(\mathbf{x}_t, \mathbf{x}_{t-1})} [\mathbf{y}_t | \mathbf{x}_t^{s_1}, \mathbf{x}_{t-1}^{s_2}] \quad (2)$$

where  $p(\mathbf{x}_t, \mathbf{x}_{t-1})$  is the joint distribution of  $(\mathbf{x}_t, \mathbf{x}_{t-1})$  and  $\mathbf{x}_t^{s_1}, \mathbf{x}_{t-1}^{s_2}$  are independent realizations of the forward process:

$$d\mathbf{x}^s = \mathbf{f}(\mathbf{x}^s, s) ds + g(s) d\mathbf{w}^s, \quad s \in [0, s_i] \quad i = 1, 2$$

with initial conditions  $\mathbf{x}_t^0 = \mathbf{x}_t, \mathbf{x}_{t-1}^0 = \mathbf{x}_{t-1}$  respectively. It is important to note that although the forward processes are independent,  $\mathbf{x}_t^{s_1}$  and  $\mathbf{x}_{t-1}^{s_2}$  are not independent since the initial conditions are drawn from their joint distribution. This is the fundamental mathematical object underlying our method that allows a tradeoff between *conditional approximation error* and *OOD error*. The motivation for the

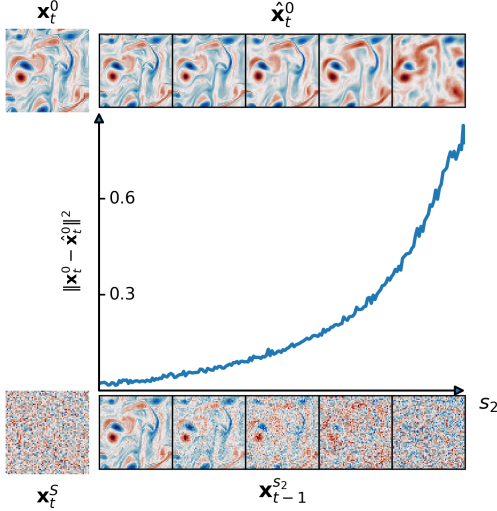


Figure 3. The x-axis corresponds to the diffusion time of the forward process for the conditional variable. The images below the x-axis are realizations of the forward process with the same initial condition  $\mathbf{x}_{t-1}^0$  at different times  $s$ . The images in the top row are in direct correspondence with the images below via an estimator of the *multi-noise-level denoising oracle*  $\hat{\mathbf{x}}_t^0 = \mathbf{D}_\theta(\mathbf{x}_t^s, \mathbf{x}_{t-1}^s)$ . The y-axis in the  $L^2$  distance between the denoised image and the original image. The degradation in denoising accuracy and the smoothing of fields with higher noise injection in the conditional variable align with the theory.

*multi-noise-level denoising oracle* is analogous to the trade-off between conditional and marginal distribution discussed in Section 3. In the limit of  $s_2 \rightarrow S$ , the denoising oracle reduces to the unconditional denoising oracle as defined in equation (1). In the limit of  $s_2 \rightarrow 0$ , the denoising oracle can be interpreted as a conditional denoising oracle which corresponds to the expected value of the transition density. The interpolation of these limits is exactly the tradeoff between *approximation error* and *OOD error*. Figure 3 demonstrates the tradeoff through an estimator of the *multi-noise-level denoising oracle*.

Given the *multi-noise-level denoising oracle* and initial condition  $\hat{\mathbf{x}}_0 = \mathbf{x}_0$ , one could use it directly for generating trajectories by following the recurrence relation  $(\hat{\mathbf{x}}_t, \hat{\mathbf{x}}_{t-1}) = \mathbf{D}(\mathbf{z}_t, \mathbf{x}_{t-1}^0)$  where  $\mathbf{z}_t \sim p^1$ . However, this generates a trajectory based on point-wise estimates, and imperfect approximations of the oracle are still subject to *OOD error* as a degenerate version of the Gaussian approximation of the transition density discussed in Section 3.

In order to enable probabilistic modeling, we define the *multi-noise-level score*,  $\nabla \log p^s(\mathbf{y}_t^s)$ , to be:

$$(\nabla_{\mathbf{x}_t} \log p^s(\mathbf{y}_t^s), \nabla_{\mathbf{x}_{t-1}} \log p^s(\mathbf{y}_t^s))$$

where  $\mathbf{s} = (s_1, s_2)$ ,  $\mathbf{y}_t^s = (\mathbf{x}_t^{s_1}, \mathbf{x}_{t-1}^{s_2})$  and  $p^s(\mathbf{y}_t^s)$  is the marginal distribution of  $(\mathbf{x}_t^{s_1}, \mathbf{x}_{t-1}^{s_2})$  in the forward process. Analogous to the univariate case, we can relate the *multi-*

*noise-level denoising oracle* to the *multi-noise-level score* via:

$$\nabla \log p^s(\mathbf{y}_t^s) = -\Sigma_s^{-1}(\mathbf{y}_t - \mathbf{D}(\mathbf{x}_t^{s_1}, \mathbf{x}_{t-1}^{s_2}))$$

where  $\Sigma_s$  is a diagonal matrix with entries  $\Sigma_{s_{ii}} = \int_0^{s_i} g^2(s') ds'$ ,  $i = 1, 2$ . Then, one could consider the coupled reverse process SDEs:

$$\begin{aligned} d\mathbf{x}_t^{s_1} &= \left[ \mathbf{f}(\mathbf{x}_t^{s_1}, s_1) - g(s_1)^2 \nabla_{\mathbf{x}_t} \log p^s(\mathbf{y}_t^s) \right] ds_1 \\ &\quad + g(s_1) d\bar{\mathbf{w}}^{s_1} \\ d\mathbf{x}_{t-1}^{s_2} &= \left[ \mathbf{f}(\mathbf{x}_{t-1}^{s_2}, s_2) - g(s_2)^2 \nabla_{\mathbf{x}_{t-1}} \log p^s(\mathbf{y}_t^s) \right] ds_2 \\ &\quad + g(s_2) d\bar{\mathbf{w}}^{s_2} \end{aligned}$$

The SDEs are coupled through the *multi-noise-level score*, but it poses no constraints on the coupling of the diffusion time  $s_1$  and  $s_2$ . The evolution of the reverse process SDEs can be best understood as traversing the two-dimensional phase space of diffusion times. Given any point  $(\tilde{s}_1, \tilde{s}_2) \in \mathbb{R}^+ \times \mathbb{R}^+$ , one could start the reverse process SDEs at any  $(\mathbf{x}_t^{s_1}, \mathbf{x}_{t-1}^{s_2}) \sim p^s(\mathbf{x}_t^{s_1}, \mathbf{x}_{t-1}^{s_2})$  and end at any point  $(s_1', s_2')$ , s.t.  $s_i' \leq \tilde{s}_i$ , following monotonically decreasing curves in  $s_1$  and  $s_2$ . Many existing diffusion-based neural surrogate models can be interpreted as different strategies of traversing the phase space. Figure 2 demonstrates the corresponding evolution of the SDE under *ACDM* (Kohl et al., 2024), *thermalizer* (Pedersen et al., 2025), and *GenCast* (clean conditioning) (Price et al., 2023).

Estimating the *multi-noise-level score* can be done by minimizing the denoising score matching objective:

$$\begin{aligned} \mathcal{L}(\theta) &:= \mathbb{E}_{s_1, s_2 \sim \mathcal{U}(0, S), \mathbf{y}_t^s, \mathbf{y}^s \sim p^s(\mathbf{y}^s | \mathbf{y}_t^0)} \\ &\quad \|\nabla \log p_s(\mathbf{y}_t^s | \mathbf{y}_t^0) - \Phi_\theta(\mathbf{y}_t^s, s_1, s_2)\|^2 \end{aligned} \quad (3)$$

In Appendix C, we show that the minimizer of Equation (3) is the *multi-noise-level score* and it coincides with the minimizer of a similar objective where the *multi-noise-level score* is replaced with:

$$(\nabla_{\mathbf{x}_t} \log p^{s_1}(\mathbf{x}_t^{s_1} | \mathbf{x}_{t-1}^{s_2}), \nabla_{\mathbf{x}_{t-1}} \log p^{s_2}(\mathbf{x}_{t-1}^{s_2} | \mathbf{x}_t^{s_1}))$$

and the expectation is taken over  $(\mathbf{x}_t^{s_1}, \mathbf{x}_{t-1}^{s_2}) \sim p^s(\mathbf{x}_t^{s_1}, \mathbf{x}_{t-1}^{s_2})$ . This provides us with another perspective on the reverse process. We can consider  $\nabla_{\mathbf{x}_t} \log p^{s_1}(\mathbf{x}_t^{s_1} | \mathbf{x}_{t-1}^{s_2})$  as an approximation to the score of the transition density,  $\nabla p(\mathbf{x}_t | \mathbf{x}_{t-1})$ , and independently evolve

$$\begin{aligned} d\mathbf{x}_t^{s_1} &= \left[ \mathbf{f}(\mathbf{x}_t^{s_1}, s_1) - g(s_1)^2 \nabla_{\mathbf{x}_t} \log p^{s_1}(\mathbf{x}_t^{s_1} | \mathbf{x}_{t-1}^{s_2}) \right] ds_1 \\ &\quad + g(s_1) d\bar{\mathbf{w}}^{s_1} \end{aligned}$$

backward in time by drawing realizations of  $\mathbf{x}_{t-1}^{s_2}$  from the forward process. Analogous to the case for *multi-noise-level*

**Algorithm 1** SNS for refinement

---

**Require:** Initial state  $\mathbf{x}_0$ , trained SNS  $\Phi_\theta$ , trained surrogate model  $\Psi_\theta$

**for**  $t = 1$  **to**  $T$  **do**

$\mathbf{x}_t = \Psi_\theta(\mathbf{x}_{t-1})$

$\hat{s}_i = \Phi^{(i)}(\mathbf{x}_t, \mathbf{x}_{t-1}), \quad i = 1, 2$

$\mathbf{z}_1, \mathbf{z}_2 \sim \mathcal{N}(\mathbf{0}, \mathbf{I})$

$\mathbf{x}_t^{\hat{s}_1} = \sqrt{\alpha_{\hat{s}_1}} \mathbf{x}_t + \sqrt{1 - \alpha_{\hat{s}_1}} \mathbf{z}_1$

$\mathbf{x}_{t-1}^{\hat{s}_2} = \sqrt{\alpha_{\hat{s}_2}} \mathbf{x}_{t-1} + \sqrt{1 - \alpha_{\hat{s}_2}} \mathbf{z}_2$

$\mathbf{x}_{t-1}^s \leftarrow \mathbf{x}_{t-1}^{\hat{s}_2}$

**for**  $s = \hat{s}_2$  **to**  $0$  **do**

$\mathbf{z} \sim \mathcal{N}(\mathbf{0}, \mathbf{I})$

$\mathbf{x}_{t-1}^{s-1} = \frac{1}{\sqrt{\alpha_s}} \left( \mathbf{x}_{t-1}^s - \frac{1 - \alpha_s}{\sqrt{1 - \alpha_s}} \Phi^{(4)}(\mathbf{x}_t^{\hat{s}_1}, \mathbf{x}_{t-1}^s) \right) + \sqrt{\beta_s} \mathbf{z}$

**end for**

$\mathbf{x}_{t-1} \leftarrow \mathbf{x}_{t-1}^0$

$\mathbf{x}_t^s \leftarrow \mathbf{x}_t^{\hat{s}_1}$

**for**  $s = \hat{s}_1$  **down to**  $0$  **do**

$\mathbf{z} \sim \mathcal{N}(\mathbf{0}, \mathbf{I})$

$\mathbf{x}_t^{s-1} = \frac{1}{\sqrt{\alpha_s}} \left( \mathbf{x}_t^s - \frac{1 - \alpha_s}{\sqrt{1 - \alpha_s}} \Phi^{(3)}(\mathbf{x}_t^s, \mathbf{x}_{t-1}^s) \right) + \sqrt{\beta_s} \mathbf{z}$

**end for**

$\mathbf{x}_t \leftarrow \mathbf{x}_t^0$

**end for**

---

denoising oracle, this approximation of the score introduces a bias but provides a better guarantee in long-term performance. Once again confirming the interpretation of  $s_2$  as the variable controlling the tradeoff. This naturally raises the following question: *what is the optimal choice of starting point and traversal strategy in the reverse phase space  $(s_1, s_2)$  that best balances conditional approximation error against out-of-distribution (OOD) error?* We address this question by constructing a conditional diffusion model that estimates both the *multi-noise-level score* and the noise level all at once.

#### 4.2. Self-refining Neural Surrogate model

Given an initial condition  $\hat{\mathbf{x}}_0$  and an estimator of the *multi-noise-level score*, one may generate autoregressive snapshots by following any monotone path in diffusion-time space that starts at  $(S, \cdot)$  and terminates at  $(0, \cdot)$ . The remaining degree of freedom is the evolution of the conditioning noise level  $s_2$ . In the idealized setting, sampling from the true transition density  $p(\mathbf{x}_t | \mathbf{x}_{t-1})$  corresponds to fixing  $s_2 \equiv 0$  throughout the reverse process. However, conditioning on an unperturbed autoregressive history is precisely what leads to *distribution drift* in practice, as confirmed by our numerical experiments and previous work (Kohl et al., 2024).

To mitigate this effect, we do not assume the conditioning input to remain in-distribution during rollouts. Instead, we dynamically determine an appropriate starting point in the  $(s_1, s_2)$  phase space and evolve the reverse process toward the endpoint  $(0, 0)$ . By leveraging the *multi-noise-level score*, the model progressively refines both the current state and its conditioning, effectively transporting the autoregressive input back toward the data manifold during generation. This self-correcting mechanism motivates the name *Self-refining Neural Surrogate (SNS)*. The full algorithmic implementation is provided in the appendix; below, we give a high-level overview of the SNS framework.

We estimate the *multi-noise-level score* and the noise levels with a neural network,  $\Phi_\theta : \mathbb{R}^d \times \mathbb{R}^d \rightarrow \mathbb{R}^d \times \mathbb{R}^d \times \mathbb{R}^{2S}$ . Denoting the outputs  $\Phi_\theta^{(3)} \in \mathbb{R}^d \times \mathbb{R}^d$ ,  $(\Phi_\theta^{(1)}, \Phi_\theta^{(2)}) \in \mathbb{R}^{2S}$ , the loss function to minimize is:

$$\begin{aligned} \mathcal{L}(\theta) := & \mathbb{E}\{\|\nabla \log p_s(\mathbf{y}_t^s | \mathbf{y}_t^0) - \Phi_\theta^{(3)}(\mathbf{y}_t^s)\|^2 \\ & + \lambda \sum_{s_1, s_2} [\mathbf{1}_{s_1} \log \Phi_\theta^{(1)}(\mathbf{y}_t^s) + \mathbf{1}_{s_2} \log \Phi_\theta^{(2)}(\mathbf{y}_t^s)]\} \end{aligned} \quad (4)$$

where  $S$  is the number of discretization steps of the forward diffusion process and  $\mathbf{1}_{s_i}$  are one-hot vectors encoding the true noise levels and the expectation is taken over  $s_1, s_2 \sim U(\mathbb{N}[0, S])$ ,  $\mathbf{y}_t^s, \mathbf{y}_t^0 \sim p^s(\mathbf{y}_t^s | \mathbf{y}_t^0)$ . We find that choosing the regularization weight,  $\lambda$ , to keep the two terms on a comparable scale works well.

Given the previous autoregressive output  $\hat{\mathbf{x}}_{t-1}$ , SNS can be used directly for generation by evolving the reverse process SDE from  $(S, \Phi_\theta^{(2)}(\mathbf{d}_t))$  where  $\mathbf{d}_t = (\mathbf{z}_t, \hat{\mathbf{x}}_{t-1})$ ,  $\mathbf{z}_t \sim p^S$ . Alternatively, one could also refine the autoregressive output by evolving the reverse coupled SDEs from  $(\Phi_\theta^{(1)}(\hat{\mathbf{y}}_t), \Phi_\theta^{(2)}(\hat{\mathbf{y}}_t))$  where  $\hat{\mathbf{y}}_t = (\hat{\mathbf{x}}_t, \hat{\mathbf{x}}_{t-1})$ . Note that for refinement, the autoregressive output can be obtained by any other surrogate model. Figure 2 illustrates the phase-space traversal strategy implemented by SNS. Through numerical experiments, we found that denoising first in the conditional variable and then denoising the current frame had the best numerical performance when compared to many other candidate traversal paths. (Section B.3) We do not claim this path is optimal; rather, we suspect this advantage reflects a numerical bias in estimating the *multi-noise-level score*, and that all monotonically decreasing paths should be equivalent. We provide a proof that shows the equivalence of monotonically decreasing paths in distribution in Theorem C.1, and we leave a more detailed investigation for future work.

## 5. Numerical Considerations

We present the pseudocode for using SNS as a complementary model to provide long-term performance guarantee for fast surrogates targeting minimal *conditional approximation error* (Algorithm 1). We follow DDPM-style train-

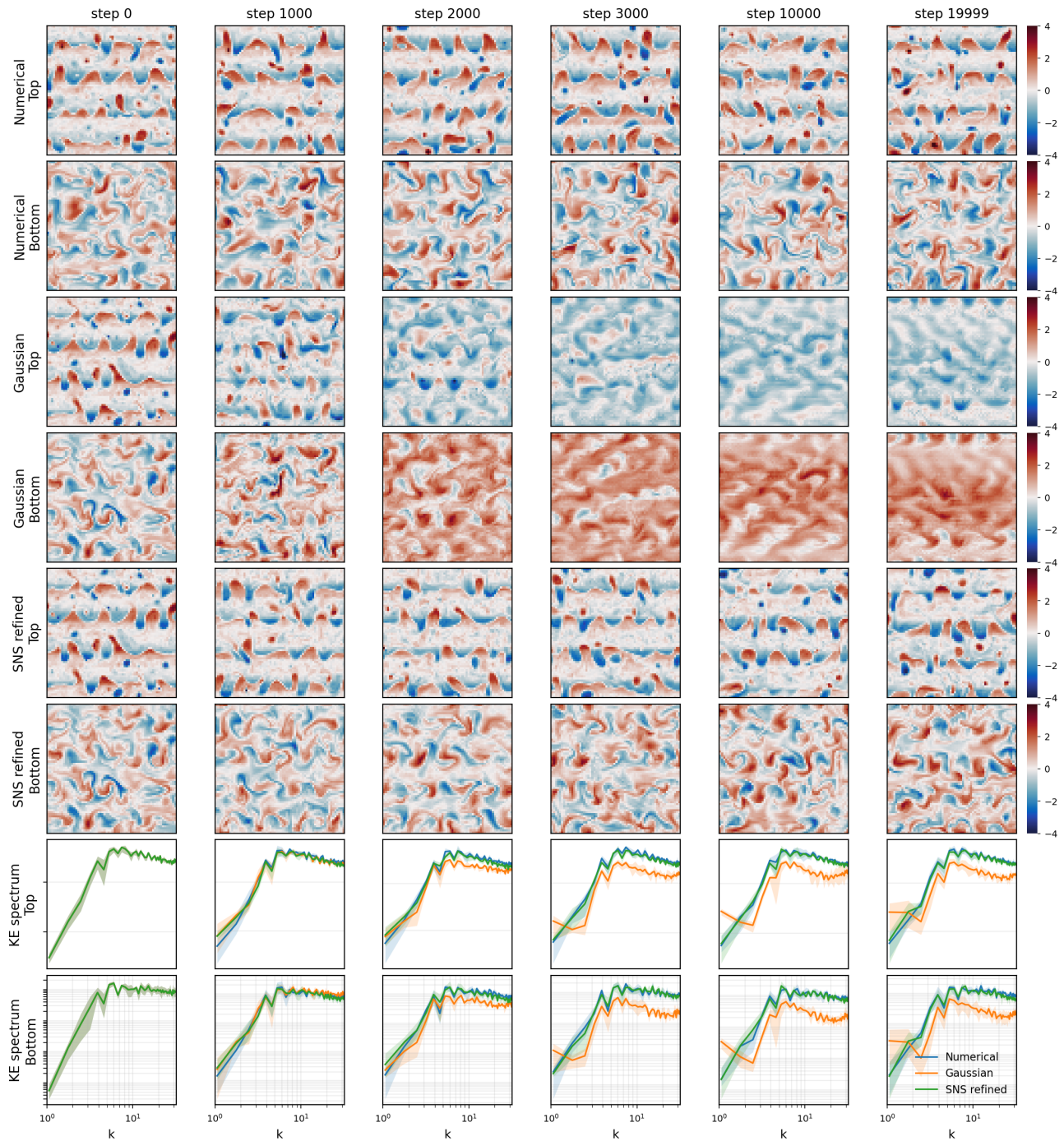


Figure 4. *Top 6 rows:* Top and bottom layer vorticity fields of the two-layer QG system from a numerical solver, Gaussian approximation of the transition density, and SNS refined trajectories for Kolmogorov flow over a trajectory of 20,000 steps. *Bottom 2 rows:* kinetic energy spectra of top and bottom layer at each timestep, averaged over 5 randomly initialized trajectories, with min-max spread shaded.

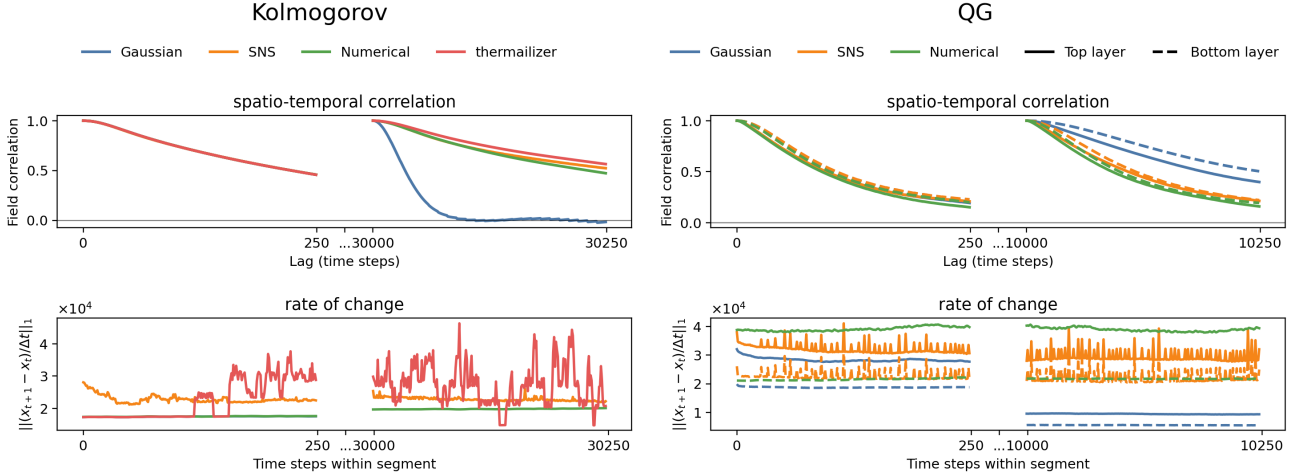


Figure 5. For a trajectory  $\mathbf{x}_t \in \mathbb{R}^d$ , we report two temporal consistency metrics. The spatio-temporal correlation at lag  $\tau$  is computed as  $C(\tau) = \langle \langle \mathbf{x}_t - \bar{\mathbf{x}}_t, \mathbf{x}_{t+\tau} - \bar{\mathbf{x}}_{t+\tau} \rangle \rangle_{t, \text{IC}} \|\mathbf{x}_t - \bar{\mathbf{x}}_t\|_2^{-1} \|\mathbf{x}_{t+\tau} - \bar{\mathbf{x}}_{t+\tau}\|_2^{-1}$  where  $\bar{\mathbf{x}}_t$  is the spatial mean of  $\mathbf{x}_t$ , and  $\langle \cdot \rangle_{t, \text{IC}}$  denotes averaging over time and initial conditions. The rate of change is computed from the discrete time derivative,  $R(t) = \|\mathbf{x}_{t+1} - \mathbf{x}_t\|_1 / \Delta t$ , and we plot the mean of  $R(t)$  over different random initial conditions. The blue curves disappear in the bottom left plot for two different reasons. From 0 to 250, the blue curve is not visible because it overlaps with the green one, indicating strong temporal accuracy of the point-wise estimate in the short rollouts. From 30000 to 30250, the blue curve is missing because the point-wise estimates are returning NaN from the blow up in scale when the distribution drifted too far away from the stationary distribution.

ing, discretizing the forward process according to the noise schedule  $\{\alpha^s, \beta^s\}_{s \in \mathbb{N}([0, S])}$  of (Ho et al., 2020). The training process and additional numerical details of *SNS* are provided in Appendix B.2.

*SNS* represents our first attempt to identify an optimal trade-off between *Conditional approximation error* and *OOD error* within the proposed framework, and in its current form it still faces several numerical challenges. First, although access to the multi-noise-level score allows the use of many existing diffusion-based methods, it also leads to a more difficult optimization problem. In particular, the *SNS* training objective departs from the conventional formulation: traditional score estimators condition on both the noisy state and the noise level, whereas *SNS* operates solely on the noisy states. As a result, *SNS* requires a finer discretization of diffusion time compared to other autoregressive conditional diffusion models during the reverse process to generate high-fidelity next-frame predictions. This substantially increases the already high computational cost of simulating the full reverse diffusion process. Consequently, all numerical results in this work rely on a refinement strategy applied to a pointwise-estimate surrogate model (e.g., a neural net that directly outputs in one pass). While this cost may be reduced in future work—potentially enabling diffusion-based models to scale to long time-horizon generation—we restrict our attention here to refinement tasks. Defining an appropriate evaluation metric for long-time simulations remains an open problem. We measure the *conditional approximation error* with temporal consistency metrics such as spatio-temporal autocorrelation and rate of change in state

space as described under Figure 5. In terms of *OOD error*, while density-based metrics such as the Kullback–Leibler divergence and Wasserstein distance are natural candidates, estimating KL divergence in high-dimensional settings is computationally prohibitive. Consequently, we restrict our evaluation to qualitative diagnostics until a principled theoretical framework for this class of tasks becomes available. In particular, we will assess the long generation consistency through the spectrum of the energy in the state space provided at the bottom of all plots.

### 5.1. Kolmogorov flow

Simulating flows governed by the Navier–Stokes equations has long been a central challenge for neural surrogate models. We first consider Kolmogorov flow, a system on which *Thermalizer* has previously demonstrated strong performance. We implement Algorithm 1 using the same point-wise surrogate model employed by *Thermalizer*, a Unet trained with a multi-step MSE objective. (Section B.2) Such models usually achieve high fidelity short-time predictions but diverge from the stationary distribution in the long run. As shown in Figure 1, *SNS* is able to maintain its diverging trajectories within the training distribution over long-time horizons.

While *ACDM* remains numerically stable, it produces fields with biased large-scale structures, leading to overly smooth solutions. It is important to note that both *Thermalizer* and *SNS* were trained with a noising schedule of 1000 diffusion steps, whereas *ACDM* was evaluated with only 200 steps,

making a direct performance comparison inherently unfair. Nevertheless, the computational cost of using *ACDM* for generation renders it impractical for long-time simulations. In contrast, the computational cost of *SNS* and *Thermalizer* is approximately two orders of magnitude lower than that of *ACDM*.

Figure 5 demonstrate the superior performance of *SNS* compared to *thermalizer* in temporal consistency. This is expected by the theory since *thermalizer* only aims to preserve marginal distributions during its projections, while *SNS* also accounts for the transition density. Although *Thermalizer* and *SNS* exhibit comparable performance in long-time simulations of Kolmogorov flow in terms of *OOD* error, we emphasize that *SNS* requires no hyperparameter tuning, whereas *Thermalizer* relies on tuning two diffusion hyperparameters,  $s_{\text{init}}$  and  $s_{\text{stop}}$ , which define the start and end points of its diffusion process.

## 5.2. Quasigeostrophic Turbulence

We also consider two-layer quasigeostrophic (QG) flows as a test case. This dynamical system is of central importance in oceanic and atmospheric sciences, where it serves as a reduced-order model for a wide range of geophysical phenomena (Majda & Qi, 2018). We evaluate all models on the jet configuration, following the experimental setup of (Ross et al., 2023).

All other neural surrogates we considered failed when trained using their respective published procedures. In particular, *ACDM* is unable to generate coherent samples even in a static denoising setting with 200 denoising steps. We did not explore *ACDM* configurations with more than 200 diffusion steps due to the computational impracticality. The publicly available implementation of *Thermalizer* fails to produce rollouts due to an internal safeguard that terminates execution when the inferred noise level exceeds a prescribed threshold.

We acknowledge that further fine-tuning of *ACDM* and *Thermalizer* can potentially result in models capable of simulating high-fidelity trajectories over long horizons. It is also worth noting that the same architecture used for the Kolmogorov flow did not succeed with the two-layer QG system at first, and a more expressive model architecture for the *multi-noise-level score* estimator was needed. We provide more numerical details and variants of *SNS* with “easier” optimization objective in Section B.

Additional videos for visualization is provided [here](#). And the code used for the numerical experiments in this paper is publicly available: [here](#).

## 6. Conclusion

We introduced *multi-noise-level denoising oracle*, a principled way to explicitly balance *conditional approximation error* and *OOD error*, formalizing heuristic-based methods for neural simulation over a long time horizon. Within this framework, we identified a central question: how to achieve an optimal tradeoff between *conditional approximation error* and *OOD error* through controlled perturbations of the conditional variable. To address this question, we proposed the *Self-refining Neural Surrogate* model (*SNS*), a conditional diffusion model which adaptively infers the optimal noise level of the conditional variable to preserve stability while respecting temporal dynamics.

Despite its conceptual succinctness, the current implementation of *SNS* is restricted by a more challenging training objective. Regardless, we demonstrated competitive performance with models designed specifically for stability guarantees in long-time simulation of the Kolmogorov flow. We also demonstrated success of *SNS* in modeling more “complicated” dynamics such as two-layer QG flows. We view *SNS* as an initial step toward a broader class of methods enabled by the multi-noise-level denoising oracle, aimed at reconciling accurate short-term prediction with long-term distributional consistency. An important direction for future work is to better understand the interplay between the temporal correlations inherent in the underlying dynamical system and the model-induced distribution drift, which we believe is critical for achieving truly long-horizon neural simulations.

## 7. Acknowledgment

The authors would like to thank Chris Pedersen, Sara Vargas, Matthieu Blanke, Fabrizio Falasca, Pavel Perezhogin, Jiarong Wu, Oliver Bühler, Rudy Morel, Jonathan Weare, Sara Shamekh, and Ryan Dù for many valuable discussions. This project is supported by Schmidt Sciences, LLC.

## 8. Impact Statement

This paper aims to help advance the field of Machine Learning. There are many potential societal consequences of our work, none of which we feel must be specifically highlighted here.

## References

Abernathey, R., rochanotes, Ross, A., Jansen, M., Li, Z., Poulin, F. J., Constantinou, N. C., Sinha, A., Balwada, D., SalahKouhen, Jones, S., Rocha, C. B., Wolfe, C. L. P., Meng, C., van Kemenade, H., Bourbeau, J., Penn, J., Busecke, J., Bueti, M., and Tobias. pyqg/pyqg: v0.7.2, May 2022. URL <https://doi.org/10.5281/>

zenodo.6563667.

- Anderson, B. D. Reverse-time diffusion equation models. *Stochastic Processes and their Applications*, 12(3):313–326, 1982.
- Bach, E., Crisan, D., and Ghil, M. Forecast error growth: A dynamic-stochastic model. *arXiv e-prints*, art. arXiv:2411.06623, November 2024. doi: 10.48550/arXiv.2411.06623.
- Batzolis, G., Stanczuk, J., Schönlieb, C., and Etmann, C. Conditional image generation with score-based diffusion models. *CoRR*, abs/2111.13606, 2021. URL <https://arxiv.org/abs/2111.13606>.
- Bi, K., Xie, L., Zhang, H., Chen, X., Gu, X., and Tian, Q. Accurate medium-range global weather forecasting with 3D neural networks. *Nature*, 619(7970):533–538, July 2023. ISSN 1476-4687. doi: 10.1038/s41586-023-06185-3.
- Bonavita, M. On some limitations of current machine learning weather prediction models. *Geophysical Research Letters*, 51(12), June 2024. ISSN 1944-8007. doi: 10.1029/2023gl107377. URL <http://dx.doi.org/10.1029/2023GL107377>.
- Cachay, S. R., Zhao, B., Joren, H., and Yu, R. DYffusion: A dynamics-informed diffusion model for spatiotemporal forecasting. In *Thirty-seventh Conference on Neural Information Processing Systems*, 2023. URL <https://openreview.net/forum?id=WRGldGm5Hz>.
- Chariker, L., Shapley, R., and Young, L.-S. Orientation Selectivity from Very Sparse LGN Inputs in a Comprehensive Model of Macaque V1 Cortex. *Journal of Neuroscience*, 36(49):12368–12384, December 2016. ISSN 0270-6474, 1529-2401. doi: 10.1523/JNEUROSCI.2603-16.2016.
- Chattopadhyay, A., Sun, Y. Q., and Hassanzadeh, P. Challenges of learning multi-scale dynamics with AI weather models: Implications for stability and one solution. *arXiv e-prints*, art. arXiv:2304.07029, April 2023. doi: 10.48550/arXiv.2304.07029.
- Dhariwal, P. and Nichol, A. Diffusion Models Beat GANs on Image Synthesis. In *Advances in Neural Information Processing Systems*, volume 34, pp. 8780–8794. Curran Associates, Inc., 2021.
- Dheeshjith, S., Subel, A., Adcroft, A., Busecke, J., Fernandez-Granda, C., Gupta, S., and Zanna, L. Samudra: An AI Global Ocean Emulator for Climate. *Geophysical Research Letters*, 52(10):e2024GL114318, May 2025. ISSN 0094-8276, 1944-8007. doi: 10.1029/2024GL114318.
- Dresdner, G., Kochkov, D., Norgaard, P., Zepeda-Núñez, L., Smith, J. A., Brenner, M. P., and Hoyer, S. Learning to correct spectral methods for simulating turbulent flows, June 2023.
- Gao, H., Kaltenbach, S., and Koumoutsakos, P. Generative learning for forecasting the dynamics of high-dimensional complex systems. *Nature Communications*, 15(1):8904, October 2024. ISSN 2041-1723. doi: 10.1038/s41467-024-53165-w.
- Ho, J. and Salimans, T. Classifier-free diffusion guidance. *arXiv preprint arXiv:2207.12598*, 2022.
- Ho, J., Jain, A., and Abbeel, P. Denoising diffusion probabilistic models. *ArXiv*, abs/2006.11239, 2020. URL <https://api.semanticscholar.org/CorpusID:219955663>.
- Ijspeert, A. J., Nakanishi, J., Hoffmann, H., Pastor, P., and Schaal, S. Dynamical Movement Primitives: Learning Attractor Models for Motor Behaviors. *Neural Computation*, 25(2):328–373, February 2013. ISSN 0899-7667. doi: 10.1162/NECO\_a.00393.
- Jiang, R., Lu, P. Y., Orlova, E., and Willett, R. Training neural operators to preserve invariant measures of chaotic attractors. In *Thirty-seventh Conference on Neural Information Processing Systems*, 2023. URL <https://openreview.net/forum?id=8xx0pyMOW1>.
- Karras, T., Aittala, M., Aila, T., and Laine, S. Elucidating the design space of diffusion-based generative models. *Advances in neural information processing systems*, 35: 26565–26577, 2022.
- Kochkov, D., Smith, J. A., Alieva, A., Wang, Q., Brenner, M. P., and Hoyer, S. Machine learning–accelerated computational fluid dynamics. *Proceedings of the National Academy of Sciences*, 118(21), May 2021. ISSN 1091-6490. doi: 10.1073/pnas.2101784118. URL <http://dx.doi.org/10.1073/pnas.2101784118>.
- Kochkov, D., Yuval, J., Langmore, I., Norgaard, P., Smith, J., Mooers, G., Klöwer, M., Lottes, J., Rasp, S., Düben, P., Hatfield, S., Battaglia, P., Sanchez-Gonzalez, A., Willson, M., Brenner, M. P., and Hoyer, S. Neural general circulation models for weather and climate. *Nature*, 632(8027):1060–1066, August 2024. ISSN 1476-4687. doi: 10.1038/s41586-024-07744-y.
- Kohl, G., Chen, L.-W., and Thuerey, N. Benchmarking Autoregressive Conditional Diffusion Models for Turbulent Flow Simulation, December 2024.
- Kurth, T., Subramanian, S., Harrington, P., Pathak, J., Mardani, M., Hall, D., Miele, A., Kashinath, K., and

- Anandkumar, A. Fourcastnet: Accelerating global high-resolution weather forecasting using adaptive fourier neural operators. In *Proceedings of the Platform for Advanced Scientific Computing Conference, PASC '23*, New York, NY, USA, 2023. Association for Computing Machinery. ISBN 9798400701900. doi: 10.1145/3592979.3593412. URL <https://doi.org/10.1145/3592979.3593412>.
- Lewy, H., Friedrichs, K., and Courant, R. Über die partiellen differenzgleichungen der mathematischen physik. *Mathematische Annalen*, 100:32–74, 1928. URL <http://eudml.org/doc/159283>.
- Li, Z., Kovachki, N. B., Azizzadenesheli, K., Liu, B., Bhattacharya, K., Stuart, A., and Anandkumar, A. Fourier Neural Operator for Parametric Partial Differential Equations. In *International Conference on Learning Representations*, October 2020.
- Lippe, P., Veeling, B. S., Perdikaris, P., Turner, R. E., and Brandstetter, J. PDE-refiner: Achieving accurate long rollouts with neural PDE solvers. In *Thirty-seventh Conference on Neural Information Processing Systems*, 2023. URL <https://openreview.net/forum?id=Qv646811WS>.
- Lorenz, E. N. Deterministic Nonperiodic Flow. *Journal of the Atmospheric Sciences*, March 1963. ISSN 1520-0469.
- Lusch, B., Kutz, J. N., and Brunton, S. L. Deep learning for universal linear embeddings of nonlinear dynamics. *Nature Communications*, 9(1):4950, November 2018. ISSN 2041-1723. doi: 10.1038/s41467-018-07210-0.
- Majda, A. J. and Qi, D. Strategies for reduced-order models for predicting the statistical responses and uncertainty quantification in complex turbulent dynamical systems. *SIAM Review*, 60(3):491–549, 2018. doi: 10.1137/16M1104664.
- Nathaniel, J. and Gentine, P. Generative emulation of chaotic dynamics with coherent prior. *Computer Methods in Applied Mechanics and Engineering*, 448:118410, January 2026. ISSN 0045-7825. doi: 10.1016/j.cma.2025.118410.
- Parthipan, R., Anand, M., Christensen, H. M., Hosking, J. S., and Wischik, D. J. Defining error accumulation in ML atmospheric simulators. *arXiv e-prints*, art. arXiv:2405.14714, May 2024. doi: 10.48550/arXiv.2405.14714.
- Pathak, J., Subramanian, S., Harrington, P., Raja, S., Chatopadhyay, A., Mardani, M., Kurth, T., Hall, D., Li, Z., Azizzadenesheli, K., Hassanzadeh, P., Kashinath, K., and Anandkumar, A. FourCastNet: A Global Data-driven High-resolution Weather Model using Adaptive Fourier Neural Operators, February 2022.
- Pedersen, C., Zanna, L., and Bruna, J. Thermalizer: Stable autoregressive neural emulation of spatiotemporal chaos. In *Forty-Second International Conference on Machine Learning*, June 2025.
- Price, I., Sanchez-Gonzalez, A., Alet, F., Andersson, T. R., El-Kadi, A., Masters, D., Ewalds, T., Stott, J., Mohamed, S., Battaglia, P., et al. Gencast: Diffusion-based ensemble forecasting for medium-range weather. *arXiv preprint arXiv:2312.15796*, 2023.
- Robbins, H. E. An empirical bayes approach to statistics. In *Breakthroughs in Statistics: Foundations and basic theory*, pp. 388–394. Springer, 1992.
- Ronneberger, O., Fischer, P., and Brox, T. U-Net: Convolutional Networks for Biomedical Image Segmentation, May 2015.
- Ross, A., Li, Z., Perezhogin, P., Fernandez-Granda, C., and Zanna, L. Benchmarking of Machine Learning Ocean Subgrid Parameterizations in an Idealized Model. *Journal of Advances in Modeling Earth Systems*, 15(1):e2022MS003258, 2023. ISSN 1942-2466. doi: 10.1029/2022MS003258.
- Salimans, T. and Ho, J. Progressive distillation for fast sampling of diffusion models, 2022. URL <https://arxiv.org/abs/2202.00512>.
- Schiff, Y., Wan, Z. Y., Parker, J. B., Hoyer, S., Kuleshov, V., Sha, F., and Zepeda-Núñez, L. Dyslim: Dynamics stable learning by invariant measure for chaotic systems. *arXiv preprint arXiv:2402.04467*, 2024.
- Shehata, Y., Holzschuh, B., and Thuerey, N. Improved sampling of diffusion models in fluid dynamics with tweedie’s formula. In *The Thirteenth International Conference on Learning Representations*, 2025. URL <https://openreview.net/forum?id=0FbzC7B9xI>.
- Sohl-Dickstein, J. N., Weiss, E. A., Maheswaranathan, N., and Ganguli, S. Deep unsupervised learning using nonequilibrium thermodynamics. *ArXiv*, abs/1503.03585, 2015. URL <https://api.semanticscholar.org/CorpusID:14888175>.
- Song, Y. and Ermon, S. Generative modeling by estimating gradients of the data distribution. *Advances in neural information processing systems*, 32, 2019.
- Song, Y., Dhariwal, P., Chen, M., and Sutskever, I. Consistency Models. In *Proceedings of the 40th International Conference on Machine Learning*, pp. 32211–32252. PMLR. URL <https://proceedings.mlr.press/v202/song23a.html>.

- Song, Y., Sohl-Dickstein, J., Kingma, D. P., Kumar, A., Ermon, S., and Poole, B. Score-Based Generative Modeling through Stochastic Differential Equations. In *International Conference on Learning Representations*, October 2020.
- Stachenfeld, K., Fielding, D. B., Kochkov, D., Cranmer, M., Pfaff, T., Godwin, J., Cui, C., Ho, S., Battaglia, P., and Sanchez-Gonzalez, A. Learned simulators for turbulence. In *International Conference on Learning Representations*, 2022. URL <https://openreview.net/forum?id=msRBojTz-Nh>.
- Subel, A. and Zanna, L. Building Ocean Climate Emulators, March 2024.
- Um, K., Brand, R., Fei, Y. R., Holl, P., and Thuerey, N. Solver-in-the-loop: Learning from differentiable physics to interact with iterative PDE-solvers. In Larochelle, H., Ranzato, M., Hadsell, R., Balcan, M., and Lin, H. (eds.), *Advances in Neural Information Processing Systems*, volume 33, pp. 6111–6122. Curran Associates, Inc., 2020.
- Vlachas, P. R., Pathak, J., Hunt, B. R., Sapsis, T. P., Girvan, M., Ott, E., and Koumoutsakos, P. Backpropagation algorithms and Reservoir Computing in Recurrent Neural Networks for the forecasting of complex spatiotemporal dynamics. *Neural Networks*, 126:191–217, June 2020. ISSN 0893-6080. doi: 10.1016/j.neunet.2020.02.016.
- Zhang, L., Cai, S., Li, M., Wetzstein, G., and Agrawala, M. Frame context packing and drift prevention in next-frame-prediction video diffusion models. In *The Thirty-ninth Annual Conference on Neural Information Processing Systems*, 2025. URL <https://openreview.net/forum?id=J8JCF64aEn>.

## A. Dynamical Systems

We provide here an overview of the dynamical systems on which we validate our method. For a more thorough description, please refer to (Pedersen et al., 2025; Ross et al., 2023).

### A.1. Kolmogorov Flow

The governing PDEs for the system are the 2D incompressible Navier-Stokes equations with sinusoidal forcing:

$$\begin{aligned}\partial_t \mathbf{u} + (\mathbf{u} \cdot \nabla) \mathbf{u} &= \nu \nabla^2 \mathbf{u} - \frac{1}{\rho} \nabla p + \mathbf{f} \\ \nabla \cdot \mathbf{u} &= 0\end{aligned}$$

where  $\mathbf{u} = (u, v)$  is the two dimensional velocity field,  $\nu$  is the kinematic viscosity,  $\rho$  is the fluid density,  $p$  is the pressure, and  $\mathbf{f}$  is an external forcing term. We choose the constant sinusoidal forcing  $\mathbf{f} = (\sin(4y), 0)$  as done in (Kochkov et al., 2021). Following (Pedersen et al., 2025), we set  $p = 1, \nu = 0.001$  which corresponds to a Reynolds number  $\text{Re} = 10,000$ . Defining the vorticity as the 2D curl of the velocity field, i.e.  $\omega := \nabla_H \times \mathbf{u}$ . One can obtain the vorticity equation by taking the curl of the above equations:

$$\partial_t \omega + \mathbf{u} \cdot \nabla \omega = \nu \nabla^2 \omega + (\nabla \times \mathbf{f}) \cdot \hat{\mathbf{z}}.$$

The equations are solved using the pseudo-spectral method with periodic boundary conditions from the open-source code `jax-cfd` (Dresdner et al., 2023). All results presented in this paper are based on the vorticity fields.

### A.2. Two Layer Quasigeostrophic Equations

For a two-layer fluid, defining the potential vorticity to be:

$$q_i = \nabla^2 \psi_i + (-1)^i \frac{f_0^2}{g' H_m} (\psi_1 - \psi_2), m \in \{1, 2\}, \quad (5)$$

where  $i = 1$  and  $i = 2$  denote the upper layer and the lower layer, respectively.  $H_i$  is the average depth of the layer,  $\psi$  is the streamfunction, and  $\mathbf{u}_i = \nabla^\perp \psi_i$ .  $f_0$  is the Coriolis frequency. The time evolution of the system is given by

$$\partial_t q_i + J(\psi_i, q_i) + \beta_i \partial_x \psi_i + U_i \partial_x q_i = -\delta_{i,2} r \nabla^2 \psi_i + \text{ssd} \quad (6)$$

where  $U_i$  is the mean flow in  $x$ ,  $\beta_i$  accounts for the beta effect,  $r$  is the bottom drag coefficient, and  $\delta_{i,2}$  is the Kronecker delta. We set the parameters following the jet configuration in (Ross et al., 2023) and solve the equations with `pyqg` with numerical timestep  $\delta t = 3600.0$ . (Abernathey et al., 2022) The physical time step in Figure 9 are subsampled by a factor of ten so the physical time step is  $\Delta t = 36000.0$ .

## B. Numerical details

### B.1. Model Architecture

All models are based on a U-Net style encoder–decoder architecture (Ronneberger et al., 2015) implemented as a residual U-Net with multi-scale skip connections. For the *multi-noise-level score* estimator, two auxiliary regression heads are attached to the bottleneck of the U-Net as done by (Pedersen et al., 2025).

The network first projects the inputs to a 64-channel feature map using a  $3 \times 3$  convolution with circular padding, followed by GELU activations throughout the network. At the bottleneck, the model applies two residual blocks operating on 512-channel feature maps. The decoder mirrors the encoder structure, using transposed convolutions ( $4 \times 4$ , stride 2) for upsampling and concatenating the corresponding encoder features via skip connections. Each decoder stage applies a residual block to fuse the upsampled and skip-connected features, progressively reducing the number of channels back to 64. In addition, the model used for the *multi-noise-level score* estimator of the QG flows has attention heads attached to the bottleneck layer. The model did not work well without this addition.

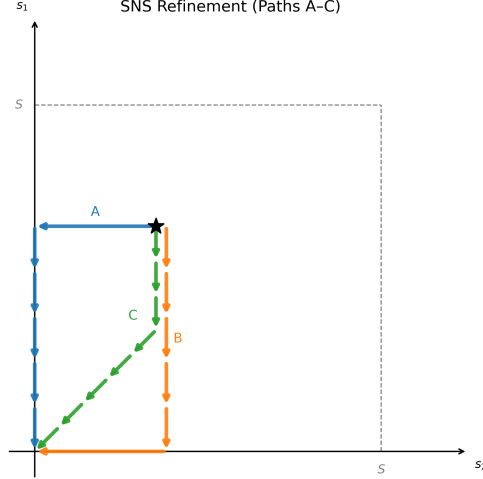


Figure 6. Different reasonable traversal strategies in the reverse SDE phase space

## B.2. Training

The training of the Gaussian approximation,  $p_\theta$ , of the transition density with point-wise estimate mean and fixed variance is done via minimizing the multi-step mean squared error on the residuals of the snapshots, i.e.

$$\mathcal{L}(\theta) = \frac{1}{N} \sum_{k=1}^N \sum_{t=0}^{L-1} \|\Psi_\theta(\mathbf{x}_t^k) - (\mathbf{x}_{t+1}^k - \mathbf{x}_t^k) + \sigma \mathbf{z}\|^2.$$

where  $\mathbf{z} \in \mathcal{N}(0, I)$ ,  $p_\theta = \mathcal{N}(\Psi_\theta, \sigma^2 I)$ . We follow the training configuration proposed by (Pedersen et al., 2025) to obtain a similar baseline model.

We train SNS using the DDPM style objective with 440,000 training pair  $\mathbf{y}_t = (\mathbf{x}_t, \mathbf{x}_{t-1})$ . We choose  $\{\beta^s\}_{s=1}^S$  to be the cosine variance schedule as proposed in (Ho et al., 2020) with  $\alpha^s = 1 - \beta^s$  and  $\bar{\alpha}^s = \prod_{k=1}^s \alpha^k$ . The forward diffusion process has the transition density:

$$q(x^s | x^0) = \mathcal{N}\left(\sqrt{\bar{\alpha}^s} x^0, (1 - \bar{\alpha}^s)I\right),$$

which allows sampling  $x_t^s$  in closed form as

$$x_t^{s_1} = \sqrt{\bar{\alpha}^{s_1}} x_t^0 + \sqrt{1 - \bar{\alpha}^{s_1}} \epsilon, \quad x_{t-1}^{s_2} = \sqrt{\bar{\alpha}^{s_2}} x_{t-1}^0 + \sqrt{1 - \bar{\alpha}^{s_2}} \epsilon', \quad \epsilon, \epsilon' \sim \mathcal{N}(0, I).$$

We noise the inputs to the neural net independently with  $s_1, s_2 \sim \mathcal{U}(1, S)$ , and the loss function we minimize is:

$$\mathcal{L}(\theta) := \mathbb{E}\{\|(\epsilon, \epsilon') - \Phi_\theta^{(3)}(\mathbf{y}_t^s)\|^2\} + \lambda \sum_{s_1, s_2} [\mathbf{1}_{s_1} \log \Phi_\theta^{(1)}(\mathbf{y}_t^s) + \mathbf{1}_{s_2} \log \Phi_\theta^{(2)}(\mathbf{y}_t^s)]$$

where the terms were defined before Equation (4). The minimizer gives us access to the *multi-noise-level score* with:

$$\epsilon = -\sqrt{1 - \bar{\alpha}_t} \nabla_{x_t} \log q(x^s | x^0).$$

We use AdamW with a learning rate of  $5e-4$  and set the weighting parameter  $\lambda = 0.1$ . Each training run requires approximately two days on a single NVIDIA H200 GPU, using a U-Net with 73,727,522 trainable parameters. Empirically, we find that augmenting the input with a sample from the invariant measure improves convergence, even though the trained model ultimately exhibits negligible dependence on this signal, indicating that its benefit is primarily during the early stages of training.

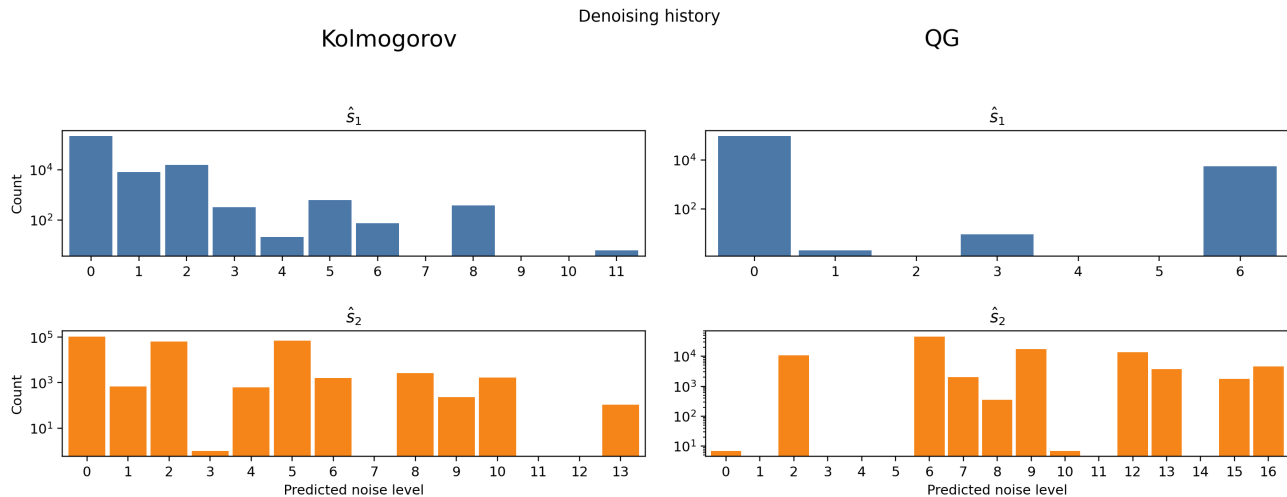


Figure 7. Histogram of denoising history for the numerical experiments in the main text

---

**Algorithm 2** SNS for generation

**Require:** Initial state  $\mathbf{x}_0$ , trained SNS  $\Phi_\theta$

**for**  $t = 1$  **to**  $T$  **do**

$$\hat{\mathbf{x}}_t, \mathbf{z} \sim \mathcal{N}(\mathbf{0}, \mathbf{I})$$

$$\hat{s}_2 = \Phi^{(2)}(\hat{\mathbf{x}}_t, \hat{\mathbf{x}}_{t-1})$$

$$\mathbf{x}_{t-1}^{\hat{s}_2} = \sqrt{\bar{\alpha}_{\hat{s}_2}} \mathbf{x}_{t-1} + \sqrt{1 - \bar{\alpha}_{\hat{s}_2}} \mathbf{z}$$

**for**  $s = S$  **to**  $0$  **do**

$$\mathbf{z}^s \sim \mathcal{N}(\mathbf{0}, \mathbf{I})$$

$$\hat{\mathbf{x}}_t^s = \frac{1}{\sqrt{\alpha_s}} \left( \hat{\mathbf{x}}_t^s - \frac{1 - \alpha_s}{\sqrt{1 - \alpha_s}} \Phi^{(3)}_\theta(\hat{\mathbf{x}}_t^s, \hat{\mathbf{x}}_{t-1}^{\hat{s}_2}) \right) + \sqrt{\beta_s} \mathbf{z}^s$$

**end for**

**end for**

---

### B.3. SNS Traversal Strategies

Mathematically, all continuous transversal strategies that end at the point  $(0, 0)$  following a monotonically decreasing path satisfy the reverse process SDE. Thus, it appears to be that there should be no difference between different choices of traversal. Figure 8 shows some reasonable traversal strategies in the reverse process phase space. Through numerical experiments, the most robust strategy appears to be path A in Figure 8. Despite numerical impracticality, we still present Algorithm 2 for using SNS to directly generate next state prediction.

We also provide a histogram of the denoising steps associated with the two numerical experiments presented in the main text in Figure 7. It is worth noting that, in practice, one could choose an activation threshold for the algorithms presented, i.e. SNS only starts denoising when a certain noise level is reached. This can improve the inference time of SNS while preserving most of its performance due to the extremely high signal-to-noise ratio at small noise levels.

### B.4. SNS Variants

We consider conditioning the *multi-noise-level denoising oracle*  $\mathbf{D}(\mathbf{x}_t^{s_1}, \mathbf{x}_{t-1}^{s_2})$  on a snapshot from the past,  $\mathbf{x}_{t-r}$ . When  $r \gg 1$ , the conditional denoising oracle recovers the unconditional oracle due to the chaotic nature of the underlying system. Similarly, in case when  $r = 1$ , the conditional denoising oracle also reduces to the unconditional case as a consequence of the Markovian property of the dynamics.

The regime of interest is when  $\mathbf{x}_{t-1}$  is perturbed by noise and  $r$  is chosen such that  $\mathbf{x}_{t-r}$  remains partially coupled to  $\mathbf{x}_{t-1}$ , but is not trivially redundant. In this setting, the parameter  $r$  can be interpreted as controlling the error trade-off. Analogous to the SNS procedure for estimating the noise level of  $\mathbf{x}_{t-1}^{s_2}$ , one could in principle estimate how far back in the trajectory one must condition in order to sufficiently weaken temporal dependence while maintaining numerical stability.

This alternative approach is considerably more challenging to implement, as it requires access to historical trajectory data. In practice, storage of long trajectories as training data may already be computationally demanding. Nevertheless, we empirically observe that providing a noise-free past frame at a predetermined lag,  $r$ , as an auxiliary conditioning signal substantially simplifies the optimization problem.

The key challenge lies in selecting a conditioning frame that is neither too close to the present (leading to excessive dependence) nor too distant (resulting in insufficiently informative conditioning). We keep this discussion informal, as the appropriate choice of  $r$  is heuristic and system-dependent. In our experiments, conditioning on a clean frame 100 steps in the past consistently improved optimization performance and was effective for stably simulating the two layer quasigeostrophic system using the same architecture backbone used for the Kolmogorov flow. (Figure 9)

## C. Proofs

**Theorem C.1** (Equivalence between monotonic traversal strategies). *Starting from an initial point  $(\mathbf{x}_t^{s_1^0}, \mathbf{x}_{t-1}^{s_2^0})$ , consider a discretized traversal path in reverse process phase space :  $\{(s_1^k, s_2^k)\}_{k=0}^N$ , with  $(s_1^0, s_2^0)$  the starting point and  $(s_1^N, s_2^N) = (0, 0)$ . Assume the path is monotonically decreasing in each coordinate:  $s_i^{k+1} \leq s_i^k$ ,  $i = 1, 2$ . Let  $(\mathbf{x}_t^{s_1^k}, \mathbf{x}_{t-1}^{s_2^k})$  evolve according to the coupled reverse SDE defined by the multi-noise-level score. Then the resulting joint distribution of the initial and terminal state*

$$p(\mathbf{x}_t^{s_1^N}, \mathbf{x}_{t-1}^{s_2^N}, \mathbf{x}_t^{s_1^0}, \mathbf{x}_{t-1}^{s_2^0})$$

is independent of the particular traversal path in reverse process phase space, i.e for any two monotonically decreasing paths

$$\{(s_1^k, s_2^k)\}_{k=0}^N, \quad \{(s_1'^k, s_2'^k)\}_{k=0}^{N'}$$

connecting  $(s_1^0, s_2^0)$  to  $(s_1^N, s_2^N)$ , the random variables generated by the reverse coupled SDE satisfy

$$p(\mathbf{x}_t^{s_1^N}, \mathbf{x}_{t-1}^{s_2^N}, \mathbf{x}_t^{s_1^0}, \mathbf{x}_{t-1}^{s_2^0}) = p(\mathbf{x}_t^{s_1'^N}, \mathbf{x}_{t-1}^{s_2'^N}, \mathbf{x}_t^{s_1^0}, \mathbf{x}_{t-1}^{s_2^0}),$$

*Proof.* Fix a monotonically decreasing discrete path in reverse process phase space

$$\{(s_1^k, s_2^k)\}_{k=0}^N, \quad (s_1^0, s_2^0) \rightarrow (s_1^N, s_2^N) = (0, 0), \quad s_i^{k+1} \leq s_i^k.$$

Since the path is monotonically decreasing, we can parametrize this path with  $u \in [0, 1]$  and define

$$u \mapsto \mathbf{s}(u) := (s_1(u), s_2(u)), \quad s_i(\cdot) \text{ nonincreasing}, \quad \mathbf{s}(0) = (s_1^0, s_2^0), \quad \mathbf{s}(1) = (0, 0),$$

such that the discretization points are contained in the image  $\{\mathbf{s}(u) : u \in [0, 1]\}$  (e.g. take  $s_i(u)$  piecewise linear through  $\{s_i^k\}$ ). Define the coupled state along the path by the single path-parameterized random variable

$$\mathbf{Y}_u := (\mathbf{x}_t^{s_1(u)}, \mathbf{x}_{t-1}^{s_2(u)}).$$

then the increments  $ds_1$  and  $ds_2$  along the path can be written as

$$ds_1 = \dot{s}_1(u) du, \quad ds_2 = \dot{s}_2(u) du, \quad \dot{s}_i(u) \leq 0$$

Substituting these relations into the coupled reverse SDE yields a single SDE in the parameter  $u$  for  $\mathbf{Y}_u$  (interpreting the stochastic integrals componentwise with respect to the time-changed Brownian motions):

$$\begin{aligned} d\mathbf{x}_t^{s_1(u)} &= \left[ \mathbf{f}(\mathbf{x}_t^{s_1(u)}, s_1(u)) - g(s_1(u))^2 \nabla_{\mathbf{x}_t} \log p^{\mathbf{s}(u)}(\mathbf{y}_t^{\mathbf{s}(u)}) \right] \dot{s}_1(u) du \\ &\quad + g(s_1(u)) d\bar{\mathbf{w}}^{s_1(u)}, \\ d\mathbf{x}_{t-1}^{s_2(u)} &= \left[ \mathbf{f}(\mathbf{x}_{t-1}^{s_2(u)}, s_2(u)) - g(s_2(u))^2 \nabla_{\mathbf{x}_{t-1}} \log p^{\mathbf{s}(u)}(\mathbf{y}_t^{\mathbf{s}(u)}) \right] \dot{s}_2(u) du \\ &\quad + g(s_2(u)) d\bar{\mathbf{w}}^{s_2(u)}. \end{aligned}$$

Thus, following a monotone path reduces the evolution to the single random variable  $\mathbf{Y}_u$  driven by the parameter  $u$ .

Now consider the forward process applied independently to each component,

$$d\mathbf{x}^s = \mathbf{f}(\mathbf{x}^s, s) ds + g(s) d\mathbf{w}^s, \quad s \in [0, S],$$

and run it along the same monotone parametrization  $u \mapsto (s_1(u), s_2(u))$ , i.e. consider the forward path process

$$\mathbf{Y}_u^{\text{fwd}} := (\mathbf{x}_t^{s_1(u)}, \mathbf{x}_{t-1}^{s_2(u)}) \quad \text{with} \quad d\mathbf{x}_t^{s_1(u)} = \mathbf{f}(\mathbf{x}_t^{s_1(u)}, s_1(u)) ds_1(u) + g(s_1(u)) d\mathbf{w}^{s_1(u)},$$

and analogously for  $\mathbf{x}_{t-1}^{s_2(u)}$ . By construction, the reverse coupled SDE uses the multi-noise-level score  $\nabla \log p^s(\mathbf{y}_t^s)$ , which is precisely the object that defines the time-reversal of the forward marginals at each noise-level  $\mathbf{s} = (s_1, s_2)$ . Consequently, when the reverse SDE is initialized at  $\mathbf{Y}_1 = (\mathbf{x}_t^{s_1^N}, \mathbf{x}_{t-1}^{s_2^N})$ , its induced law on path space  $\{\mathbf{Y}_u : u \in [0, 1]\}$  matches (in reverse time) the law of the forward process runs along the same path. In particular, the reverse process produces the correct conditional endpoint distribution associated with that path:

$$p(\mathbf{Y}_0^{\text{bwd}}, \mathbf{Y}_1^{\text{bwd}}) = p(\mathbf{Y}_0^{\text{fwd}}, \mathbf{Y}_1^{\text{fwd}}),$$

Now take any two monotone paths  $s(u) = (s_1(u), s_2(u))$  and  $s'(u) = (s'_1(u), s'_2(u))$  connecting the same endpoints  $(s_1^0, s_2^0)$  and  $(0, 0)$ . Under the forward dynamics, the two coordinates evolve independently given their own noise levels, i.e. the law of  $\mathbf{x}_t^{s_1}$  depends only on  $s_1$  and the law of  $\mathbf{x}_{t-1}^{s_2}$  depends only on  $s_2$ , with independent driving Brownian motions. Therefore, for any such path, the forward endpoint distribution at  $(0, 0)$  factors as

$$p(\mathbf{x}_t^{s_1^0}, \mathbf{x}_{t-1}^{s_2^0}, \mathbf{x}_t^0, \mathbf{x}_{t-1}^0) = \left( p(\mathbf{x}_t^{s_1^0} \mid \mathbf{x}_t^0), p(\mathbf{x}_{t-1}^{s_2^0} \mid \mathbf{x}_{t-1}^0) \right) \otimes p(\mathbf{x}_t^0, \mathbf{x}_{t-1}^0),$$

where  $\otimes$  is element-wise multiplication. The factoring clearly does not depend on how one jointly traverses  $(s_1, s_2)$ , only on the endpoints in each coordinate.

Thus, we conclude that the reverse process generates the right distribution independent of the traversal path.  $\square$

### Equivalence of minimizers: joint score vs. conditional scores

Fix  $\mathbf{s} = (s_1, s_2) \in [0, S]^2$  and let  $\mathbf{y}_t^s := (\mathbf{x}_t^{s_1}, \mathbf{x}_{t-1}^{s_2}) \sim p^s$  denote the noised pair at noise levels  $\mathbf{s}$ . Consider the denoising score matching objective

$$\mathcal{L}_{\text{joint}}(\theta) := \mathbb{E}_{\mathbf{s} \sim \mathcal{U}(0, S)^2} \mathbb{E}_{\mathbf{y}_t^0 \sim p} \mathbb{E}_{\mathbf{y}_t^s \sim p^s(\cdot \mid \mathbf{y}_t^0)} \left\| \nabla_{\mathbf{y}} \log q_{\mathbf{s}}(\mathbf{y} \mid \mathbf{y}_t^0) - \Phi_{\theta}(\mathbf{y}_t^s, s_1, s_2) \right\|_2^2, \quad (7)$$

where  $\mathbf{y} = \mathbf{y}_t^s$  and  $p^s(\cdot \mid \cdot)$  is the forward noising kernel.

Also consider the objective

$$\mathcal{L}_{\text{cond}}(\theta) := \mathbb{E}_{\mathbf{s} \sim \mathcal{U}(0, S)^2} \mathbb{E}_{\mathbf{y}_t^s \sim p^s} \left\| \begin{pmatrix} \nabla_{\mathbf{x}_t} \log p^{s_1}(\mathbf{x}_t^{s_1} \mid \mathbf{x}_{t-1}^{s_2}) \\ \nabla_{\mathbf{x}_{t-1}} \log p^{s_2}(\mathbf{x}_{t-1}^{s_2} \mid \mathbf{x}_t^{s_1}) \end{pmatrix} - \Phi_{\theta}(\mathbf{y}_t^s, s_1, s_2) \right\|_2^2. \quad (8)$$

Then given a parametric class  $\Theta$ , the sets of minimizers coincide:

$$\arg \min_{\theta \in \Theta} \mathcal{L}_{\text{joint}}(\theta) = \arg \min_{\theta \in \Theta} \mathcal{L}_{\text{cond}}(\theta),$$

**Notation.** Let  $p^s(\mathbf{y}_t^s \mid \mathbf{y}_t^0)$  denote the forward noising kernel induced by the independent SDEs, and define the marginal

$$p^s(\mathbf{y}_t^s) := \int p(\mathbf{y}_t^0) p^s(\mathbf{y}_t^s \mid \mathbf{y}_t^0) d\mathbf{y}_t^0.$$

**Lemma C.2.** Fix  $\mathbf{s} = (s_1, s_2)$ . For any measurable  $\psi(\mathbf{y})$ , the objectives

$$\mathbb{E}_{\mathbf{y}_t^0 \sim p^0} \mathbb{E}_{\mathbf{y}_t^s \sim p^s(\cdot \mid \mathbf{y}_t^0)} \left[ \left\| \nabla_{\mathbf{y}} \log p^s(\mathbf{y}^s \mid \mathbf{y}_t^0) - \psi(\mathbf{y}) \right\|^2 \right]$$

and

$$\mathbb{E}_{\mathbf{y} \sim p^s} \left[ \|\nabla_{\mathbf{y}} \log p^s(\mathbf{y}) - \boldsymbol{\psi}(\mathbf{y})\|^2 \right]$$

have the same minimizer over  $\boldsymbol{\psi}$ , given by

$$\boldsymbol{\psi}^*(\mathbf{y}) = \nabla_{\mathbf{y}} \log p^s(\mathbf{y}^s).$$

*Proof.* Fix  $\mathbf{s}$  and abbreviate  $\mathbf{y} = \mathbf{y}_t^s$ . By the tower property of conditional expectation,

$$\mathbb{E}_{\mathbf{y}_t^0} \mathbb{E}_{\mathbf{y} | \mathbf{y}_t^0}[\cdot] = \mathbb{E}_{\mathbf{y} \sim p^s} \mathbb{E}_{\mathbf{y}_t^0 | \mathbf{y}}[\cdot].$$

Hence the first objective can be written as

$$\mathbb{E}_{\mathbf{y} \sim p^s} \mathbb{E}_{\mathbf{y}_t^0 | \mathbf{y}} \left[ \|\nabla_{\mathbf{y}} \log p^s(\mathbf{y} | \mathbf{y}_t^0) - \boldsymbol{\psi}(\mathbf{y})\|^2 \right].$$

For each fixed  $\mathbf{y}$ , the minimizer of the inner expectation is the conditional mean,

$$\boldsymbol{\psi}^*(\mathbf{y}) = \mathbb{E}_{\mathbf{y}_t^0 | \mathbf{y}} \left[ \nabla_{\mathbf{y}} \log p^s(\mathbf{y} | \mathbf{y}_t^0) \right].$$

Using the identity  $\nabla p = p \nabla \log p$ , we compute

$$\begin{aligned} \nabla_{\mathbf{y}} p^s(\mathbf{y}) &= \nabla_{\mathbf{y}} \int p(\mathbf{y}_t^0) q^s(\mathbf{y} | \mathbf{y}_t^0) d\mathbf{y}_t^0 \\ &= \int p(\mathbf{y}_t^0) p^s(\mathbf{y} | \mathbf{y}_t^0) \nabla_{\mathbf{y}} \log p^s(\mathbf{y} | \mathbf{y}_t^0) d\mathbf{y}_t^0. \end{aligned}$$

Since  $p(\mathbf{y}_t^0) p^s(\mathbf{y} | \mathbf{y}_t^0) = p^s(\mathbf{y}) p(\mathbf{y}_t^0 | \mathbf{y})$ , we obtain

$$\nabla_{\mathbf{y}} \log p^s(\mathbf{y}) = \mathbb{E}_{\mathbf{y}_t^0 | \mathbf{y}} \left[ \nabla_{\mathbf{y}} \log p^s(\mathbf{y} | \mathbf{y}_t^0) \right],$$

which proves the claim. □

**Theorem C.3** (Minimizer of the multi-noise-level DSM objective). *The minimizer of the objective (3) is given (for almost every  $\mathbf{s}$ ) by*

$$\boldsymbol{\Phi}^*(\mathbf{y}_t^s, \mathbf{s}) = \nabla_{\mathbf{y}} \log p^s(\mathbf{y}_t^s).$$

*Proof.* The objective (3) is an expectation over  $\mathbf{s} \sim \mathcal{U}(0, S)^2$  of the objectives considered in Lemma C.2. Since each  $\mathbf{s}$ -slice is minimized by  $\nabla_{\mathbf{y}} \log p_s(\mathbf{y})$ , the full objective is minimized by the same function almost everywhere in  $\mathbf{s}$ . □

**Corollary C.4** (Equivalence with conditional scores). *For  $\mathbf{y} = (\mathbf{x}_t^{s_1}, \mathbf{x}_{t-1}^{s_2})$ ,*

$$\nabla_{\mathbf{y}} \log p^s(\mathbf{y}) = \left( \nabla_{\mathbf{x}_t} \log p^{s_1}(\mathbf{x}_t^{s_1} | \mathbf{x}_{t-1}^{s_2}), \nabla_{\mathbf{x}_{t-1}} \log p^{s_2}(\mathbf{x}_{t-1}^{s_2} | \mathbf{x}_t^{s_1}) \right).$$

*Consequently, replacing the multi-noise-level score in (3) by the pair of conditional scores yields an objective with the same minimizer.*

*Proof.* By the factorization

$$\log p_s(\mathbf{x}_t^{s_1}, \mathbf{x}_{t-1}^{s_2}) = \log p^{s_1}(\mathbf{x}_t^{s_1} | \mathbf{x}_{t-1}^{s_2}) + \log p^{s_2}(\mathbf{x}_{t-1}^{s_2}),$$

the second term does not depend on  $\mathbf{x}_t^{s_1}$ , yielding the first identity. The second follows analogously. □

**Corollary C.5.** *Minimizer of conditional approximation error requires clean conditioning.*

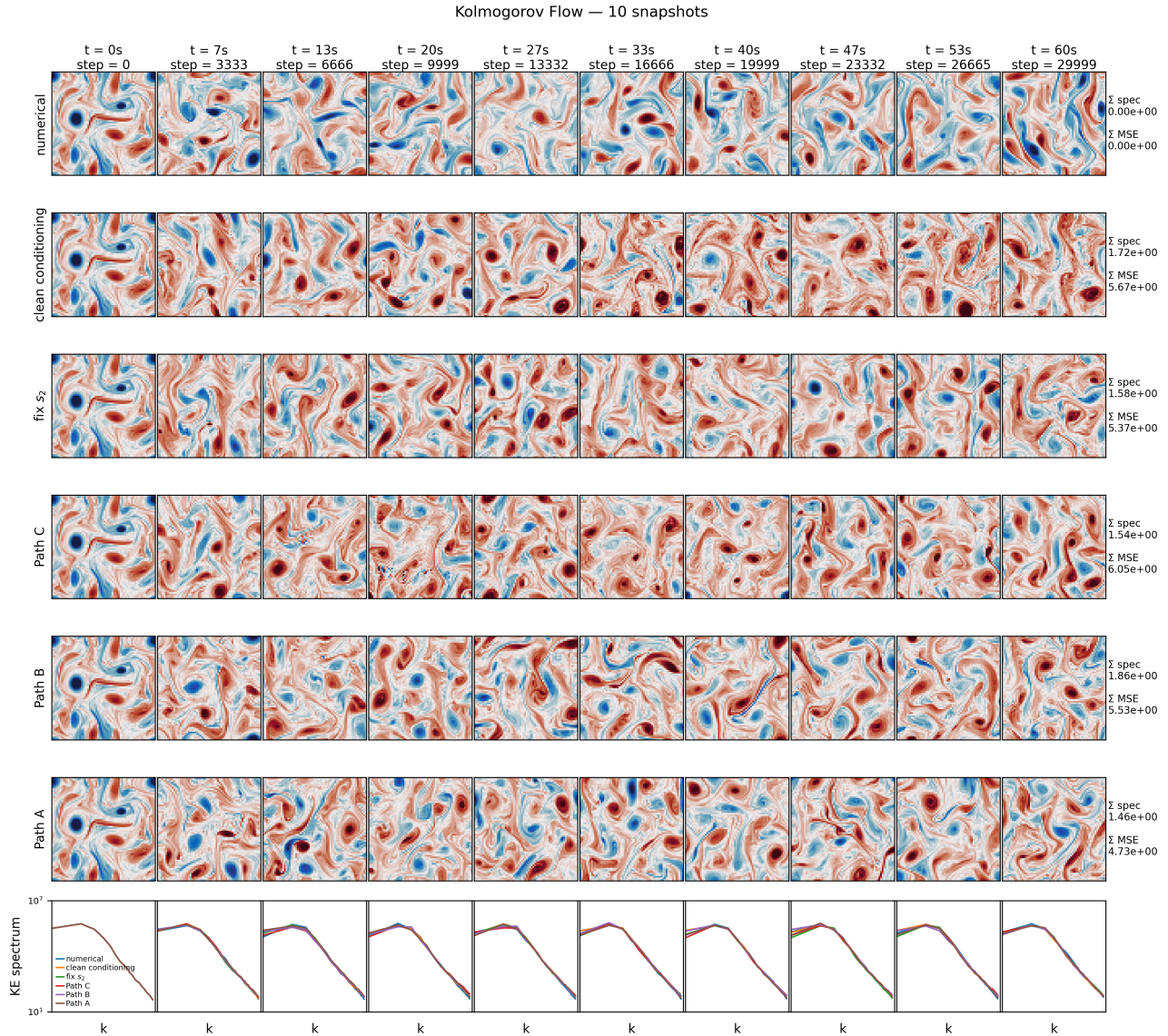


Figure 8. Each row in a rollout from the same initial condition using point-wise estimate surrogate and SMS refinement, but each following a different traversal strategy. The spectra are averaged over 20 snapshots at time  $t$  with independent initial conditions. On the right is the  $L^2$  distance between the temporal mean of numerical fields and the mean of each run, and similarly for the  $L^2$  distance between the densities.

Suppose  $d$  is the conditional KL divergence:

$$\mathcal{R}_{\text{cond}}(q) := \mathbb{E}_{x \sim \mu} \left[ \text{KL}(p(\cdot | x) \| q(\cdot | x)) \right], \quad (9)$$

where  $x = x_{t-1}$  and  $p(\cdot | x) = p(x_t | x_{t-1})$ . It is immediate that the unique minimizer (a.e. in  $x$ ) is  $q^*(\cdot | x) = p(\cdot | x)$ , with minimum value 0.

Now suppose we do *not* condition on the clean state  $x$ , but only on a corrupted observation  $\tilde{x} \sim r(\tilde{x} | x)$  (e.g. Gaussian noising). Any predictor based on the corrupted input has the form  $q(x_t | \tilde{x})$ . The best achievable predictor in this restricted class is:

$$q^*(x_t | \tilde{x}) = p(x_t | \tilde{x}) := \int p(x_t | x) p(x | \tilde{x}) dx. \quad (10)$$

Moreover, the *irreducible gap* between conditioning on  $x$  and on  $\tilde{x}$  is exactly a conditional mutual information:

$$\inf_{q(\cdot | \tilde{x})} \mathbb{E} \left[ \text{KL}(p(\cdot | x) \| q(\cdot | \tilde{x})) \right] = \mathbb{E} \left[ \text{KL}(p(\cdot | x) \| p(\cdot | \tilde{x})) \right] = I(X_t; X_{t-1} | \tilde{X}_{t-1}), \quad (11)$$

where the expectation is under the joint law  $p(x_{t-1}) p(x_t | x_{t-1}) r(\tilde{x}_{t-1} | x_{t-1})$ .

In particular, if the corruption is non-degenerate, then typically  $I(X_t; X_{t-1} | \tilde{X}_{t-1}) > 0$ , so conditioning on  $\tilde{x}_{t-1}$  cannot attain the minimum of (9). Equality holds if and only if  $\tilde{X}_{t-1}$  is a sufficient statistic for  $X_{t-1}$  with respect to  $X_t$ , i.e.  $X_t \perp X_{t-1} | \tilde{X}_{t-1}$ ; the degenerate case  $\tilde{X}_{t-1} = X_{t-1}$  recovers the clean-conditioning optimum.

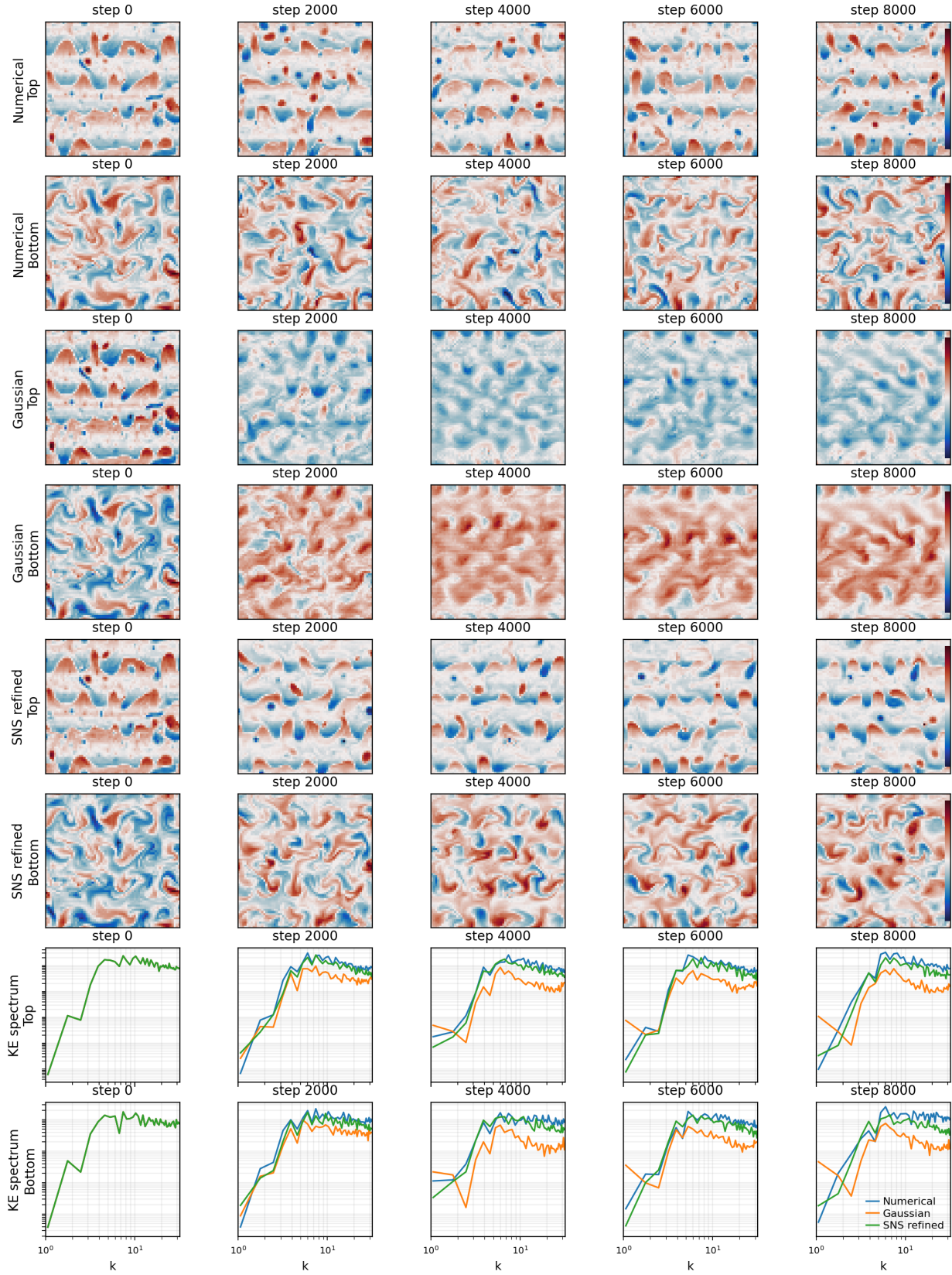


Figure 9. 2 layer Quasigeostrophic Turbulence with SNS variants